Studies of avalanche photo diodes for a calorimeter readout at a linear collider detector

Diplomarbeit
von
Hendrik Meyer

II. Institut für Experimentalphysik
Universität Hamburg
Oktober 2004

Abstract

For a future linear collider a hadronic sandwich scintillator calorimeter is foreseen as one option. This hadronic calorimeter is planned as a tracking calorimeter inside the magnetic coil. For this option, a high granularity is mandatory. One choice for a readout in high magnetic field can be an avalanche photo diode equipped detector.
In this thesis measurements of the characteristics of avalanche photo diodes are described. The homogeneity of the avalanche photodetectors have been tested and calibration measurements with a calorimeter prototype have been made in a testbeam at DESY.
An LED monitoring system for measurement stabilisation has been investigated.

Zusammenfassung

Eine Variante des hadronischen Kalorimeters für einen zukünftigen Linearbeschleuniger ist als Scintillatorkalorimeter in Schichtbauweise vorgesehen. Dieses Kalorimeter ist als Spurkalorimeter innerhalb des Magnets geplant. Für diese Variante wird eine hohe Segmentierung benötigt. Eine Option für die Auslese in einem starken Magnetfeld sind Lawinen-Photodioden (Avalanche Photodiodes, APDs).
In dieser Arbeit werden Messungen der Eigenschaften der APDs beschrieben. Die Homogenität der APDs wurde überprüft und Kalibrierungsmessungen mit einem Kalorimeterprototypen in einem Teststrahl am DESY durchgeführt. Ein LED-Kontrollsystem für die Stabilisierung von Messungen wurde entwickelt und erprobt.

Contents

1 Introduction **6**

2 The TESLA Detector **8**

2.1 Tracking Devices 9

2.2 Calorimeter 10

2.2.1 Electromagnetic Calorimeter 10

2.2.2 Hadronic Calorimeter 10

2.2.3 Particle Flow Algorithm 11

2.3 Magnet and Muon Chamber 12

3 Physics in a Calorimeter **13**

3.1 Particle Interaction with Matter 13

3.2 Electromagnetic Showers 15

3.3 Hadronic Showers 16

3.4 Sampling Calorimeter 17

3.5 Energy Resolution 17

3.6 Photodetectors 18

3.6.1 Vacuum Photo Tubes 20

3.6.2 Avalanche Photo Diodes 21

3.6.3 Silicon Photomultiplier 23

4 MiniCal Calorimeter Prototype Setup **25**

4.1 Main Structure 25

4.2 Cassettes 26

4.3 Readout 27

4.4 Preamplifier 29

4.5 Beam Setup 30

5 LED Monitoring System **32**

5.1 Setup 33

5.2 Short Term Measurements 35

5.3 Long Term Measurements 36

6 APD Studies **39**

6.1 APD Characterisation 39

6.1.1 APD Gain and Capacity 39

6.1.2 APD Homogeneity 41

6.2 APD MiniCal Data 43

6.2.1 MIP Calibration 43

6.2.2 Detector Simulation 45

6.2.3 Shower Shape Comparison 46

6.2.4 Systematic Errors 48

6.2.5 Linearity and Energy Resolution 48

7 Summary and Outlook **51**

List of Figures

1.1 Energy resolution comparison for reconstruction of W or Z bosons. . . . 7

2.1 Sketch of one quadrant of the proposed TESLA detector [3]. 9
2.2 Particle flow example. 12

3.1 Stopping power for muons in copper [23]. 14
3.2 A simple electromagnetic shower induced by a photon. 15
3.3 a) Principle scheme for APDs and SiPMs. b) Voltage dependence of the gain. 19
3.4 Working principle of a vacuum photo tube. 20
3.5 Sketch of an APD. 21
3.6 Temperature and voltage dependence for S8664-55 APDs from Hamamatsu. 22
3.7 Sketch of a SiPM structure. 23
3.8 Saturation curve for a SiPM. 24

4.1 MiniCal structure. 26
4.2 One MiniCal cassette containing 9 scintillator tiles with WLS readout. 27
4.3 Scintillator spectrum and WLS spectrum. 27
4.4 Optical way of a signal from the particle and from the LED pulse generator to the photodetector. 28
4.5 Logical way of a signal from photodetectors to the data acquisition. . . 28
4.6 MIP signal seen from photomultiplier and from APD. 29
4.7 Scheme of the trigger system. 30

5.1 LED light distributing system with one clear fibre to a PIN diode and 11 clear fibres to photodetectors. 33

5.2 (a) Spectrum of the LED light used in the monitoring system. (b) Relative spectral sensitivity of the used PIN diode. 34
5.3 (a) LED driver circuit diagram. (b) LED pulse produced with the LED driver circuit and observed with a fast PMT. 34
5.4 Relative amplitude of the LED signal recorded by 2 PIN diodes over 2 h of data taking. 35
5.5 Relative amplitude of the LED signal recorded by 2 APDs over 2 h of data taking after PIN diode correction. 35
5.6 (a) Temperature shift in a 60 h run. (b) APD shift in gain seen with the LED signal for the same run. (c) PIN diode signal to monitor LED stability. 36
5.7 (a) APD signal versus temperature. (b) APD signal and calculated curve for the given temperature. 37
5.8 (a) APD signal distribution for LED light without temperature correction. (b) APD signal corrected for LED emission changes. (c) APD signal after correcting for temperature fluctuations. 38

6.1 The gain versus bias voltage for the 33 used Hamamatsu 3×3 mm^2 APDs. 40
6.2 The capacitance for one Hamamatsu 3×3 mm^2 APD. 40
6.3 (a) Sketch of the homogeneity measurement procedure. The positions of the measurement points are shown. (b) Picture of the homogeneity measurement setup with APD and clear fibre. 41
6.4 Measured gain variation for 2 APDs at different positions. The gain is normalised. 42
6.5 Distribution of all measured points. The mean value is at 1 the width is σ=0.03. 42
6.6 MIP signal for the 12^{th} tile in the central stack as an example of MIP calibration at 3 GeV. (a) MIP peak with 11 cassettes in front. (b) MIP peak without 11 cassettes in front. 44
6.7 Ratio of two sets of calibration factors for the core tiles. 45
6.8 Flow chart of simulation implementation of photodetector physics. . . . 45
6.9 Transversal shower shape for the 5^{th} layer. 46
6.10 Longitudinal shower shape for the central tiles. 47
6.11 Energy sum for energies from 1 GeV to 6 GeV. 49
6.12 (a) Linearity for two runs with different preamplifiers. They both show the same linear behaviour. (b) Deviation from the linear curve for both preamplifiers and simulation. 50
6.13 Energy resolution. 50

Chapter 1

Introduction

There is a global consensus in the high energy physics community that the next accelerator project in particle physics needs to be an electron-positron linear collider with energy range from $\sqrt{s}$= M_Z=91 GeV up to 1 TeV. Physics goals at this International Linear Collider (ILC) include detection and study of the Higgs boson, detailed study of the top quark and precision tests of the electroweak theory. There is also a good chance to explore new physics beyond the standard model. At present there are three conceptual designs for the electron-positron linear collider and the detectors, the TESLA Project [3], the Next Linear Collider [5] and Japanese Linear Collider [4]. The community has agreed to use the superconducting technology proposed in the TESLA project for the accelerator. The studies presented here are carried out in the framework of the TESLA studies, but are applicable to the other projects, too.
In order to achieve the physics goals at the ILC, the detector has to be constructed with an excellent energy/momentum resolution and a good hermeticity, as well as efficient b-tagging and lepton identification capabilities. In the next chapter the TESLA detector concept is described.
The calorimeter is one of the most important components of the detector. The resolution of the invariant mass of multiple jet final states is essential in most of the physics studies such as studies of the electroweak couplings, where the mass of the W bosons have to be distinguished from Z bosons by means of the invariant mass. For this purpose the calorimeter should have a jet energy resolution better than $30\%\sqrt{E}$ [1] as illustrated in figure 1.1. Monte Carlo simulations demonstrated that these requirements can be met in a hadronic calorimeter of very fine longitudinal and transversal granularity leading to a huge amount of readout channels. The shower has to be reconstructed from single track identification using methods called particle flow algorithms (PFA) [10]. In chapter 2 the concept of the TESLA detector and the particle flow method is explained in brief.
The required high granularity can be achieved using scintillator tiles in a sampling calorimeter. I will describe the physics of a calorimeter and the idea of a sampling calorimeter in chapter 3. Different photodetectors used in our prototype are intro-

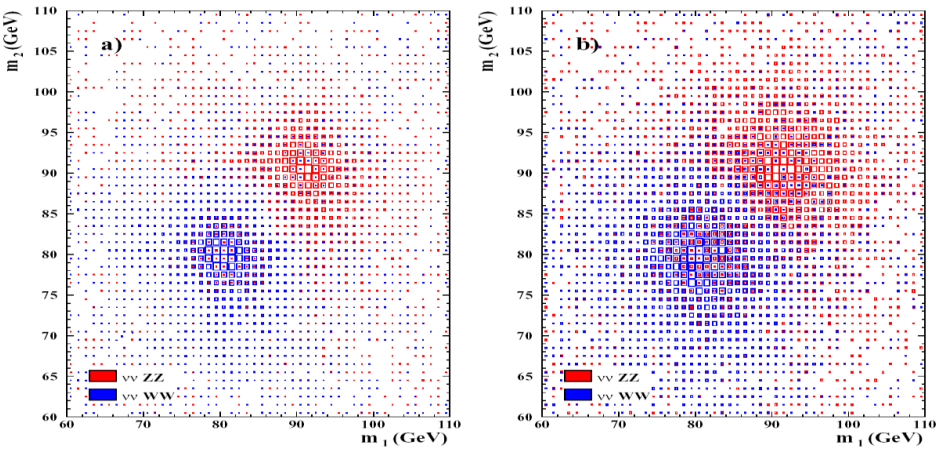

Figure 1.1: Reconstructed masses for $e^+e^- \to WW\nu\overline{\nu}$ events and $e^+e^- \to ZZ\nu\overline{\nu}$ events for a) $\Delta E/\sqrt{E}$=30% as proposed for the future ILC detector and b) $\Delta E/\sqrt{E}$=60% as achieved at the LEP experiments [3].

duced.
The concept of a scintillator hadronic calorimeter with novel semiconductor based photodetectors, Avalanche PhotoDiodes (APD) and Silicon PhotoMultipliers (SiPM), is part of the CALICE [13] research and developement (R&D) program. The photodetectors are presented in section 3.6. In order to study the hadronic shower developement a $1\,\mathrm{m}^3$ prototype of scintillator tile hadronic calorimeter will be built and tested together with a prototype of the electromagnetic calorimeter in front.
To test and optimise the hardware a small prototype has been built and operated at the DESY testbeam, the MiniCal. The MiniCal is described in chapter 4. The readout system is controlled with a LED monitoring sytem. In this thesis APD data are analysed. The temperature correction is investigated in chapter 5. The Measurement results with APD readout are presented in in chapter 6. Finaly a summary and outlook are given in chapter seven.

Chapter 2

The TESLA Detector

The physics program for a future electron-positron collider, discussed now by the high energy physics community, covers a wide kinematic range of centre of mass energies from the Z peak at 91 GeV to the TeV regime. The range allows discovery of new physics and precision measurements of standard model processes. If a light elementary Higgs particle exists, as predicted by the standard model, precise measurements of this boson demand collisions with centre of mass energies of $\sqrt{s}$ between 250 GeV and 800 GeV. Since the Higgs mechanism predicts couplings to scale with the particle masses, excellent identification capabilities of parton flavour and gauge boson type are mandatory. Direct discovery of an extended Higgs structure, of supersymmetry or the manifestation of other new physics at LHC will compel precision experiments.
In the opposite situation that no light Higgs is found, the electroweak symmetry breaking mechanism should be examined using $\sqrt{s}$=91 GeV with polarised beams.
At present there are three conceptual designs for the electron-positron linear collider detector, one small all silicon detector as proposed for the Next Linear Collider [5], a medium sized detector in the TESLA Project [3] and a large detector proposed for the Japanese Linear Collider [4]. An overview of the ongoing R&D for the detector is given in [6]. As the studies are carried out in the framework of the TESLA studies, I will give a brief overview of the TESLA detector.
The detector will have to deal with a large dynamic range in energy and the complexity of final states. The jet multiplicity will increase dramatically with respect to the previous electron-positron colliders LEP and SLC. The detector must be substantially better in four main detector issues: track momentum resolution, jet flavour tagging, energy reconstruction and hermiticity.
Figure 2.1 shows the proposed TESLA detector. The vertex detector (VTX) close to the interaction region and the intermediate tracker (SIT) are both silicon devices. As a main tracking device a Time Projection Chamber (TPC) is foreseen. An electromagnetic (ECAL) and a hadronic (HCAL) calorimeter serve for energy measurements. These inner parts are enclosed by a solenoidal coil and the flux return yoke. The outermost part of the detector is the muon detection system.

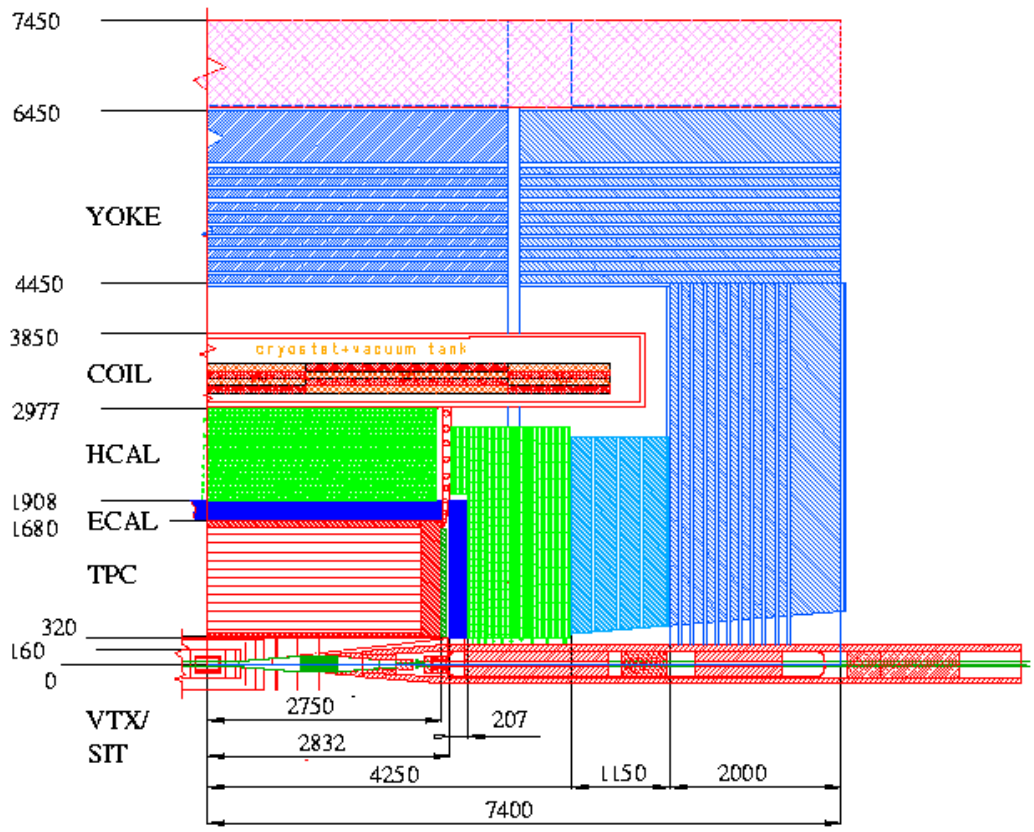

Figure 2.1: Sketch of one quadrant of the proposed TESLA detector [3].

2.1 Tracking Devices

The vertexing and tracking detectors are the nearest devices to the interaction point. The main goal of these detectors is the precise track reconstruction and the determination of the momentum from the curvature of particle tracks in the magnetic field.
The silicon vertex detectors are primarily optimised to reconstruct secondary vertices in b- and c- decays. To obtain a good reconstruction efficiency at least three detector layers are proposed.
Time Projection Chambers (TPC) allow an efficient 3-dimensional track reconstruction with many track points. In addition no massive material except support structures compromises the outer detectors.
According to the TESLA Technical Design Report [3] the transverse momentum resolution should be $\delta(1/p_t) < 5 \times 10^{-4}$ (GeV/c)$^{-1}$. Therefore a point resolution less than 150 μm is necessary. In addition, the usage of new technologies for the readout system such as Gas Electron Multiplier (GEM) foil readout is favoured. The operation principle of GEMs in a TPC is explained in [17].

2.2 Calorimeter

Reconstruction of parton four-momenta with high resolution will be a key factor for the detector. The reconstruction of parton jet energies has to be as precise as possible. The best resolution for jets is achieved using a particle flow algorithm (PFA) as explained in section 2.2.3.
Also the calorimeter has to cope with reconstruction of photons coming from secondary vertices, good time resolution to avoid event pile-up and excellent angular resolution. This is best realised in a dense and hermetic sampling calorimeter with very high granularity. The hermeticity requirement also forces to include the calorimeters inside the coil, otherwise the calorimeter performance would be degraded.

2.2.1 Electromagnetic Calorimeter

There are some options for an electromagnetic calorimeter (ECAL) planned for TESLA: One option is a tungsten sampling-calorimeter with a thickness of 24 radiation lengths. The sampling structure consists of tungsten with silicon active material, 30 layers with a radiation length of $0.4X_0$ and 10 layers of $1.2X_0$. The goal is an energy resolution of better than $10\%\frac{1}{\sqrt{E}}$. A transversal pad size of 1×1 cm^2 is planned. This design is currently investigated by [7].
Another option is an absorber-scintillator sandwich calorimeter with WLS fibre readout and three additional silicon pad planes to optimise the measurement of the shower developement. This design is currently investigated by [14].
There is an study of a lead shashlick calorimeter. The lead plates, containing 6% antimony in weight for hardness, have a thickness of 2 mm. Scintillator fibres are embedded in the lead plates. This design has been investigated by [8].

2.2.2 Hadronic Calorimeter

A sampling calorimeter as a hadronic calorimeter (HCAL) has been proposed in the TESLA technical design report. Two options are under investigation, one being a sandwich calorimeter with scintillating tiles (more classic solution), the other a digital calorimeter with RPC readout or wire chamber readout (multiple chambers). The scintillating tile solution will have a segmentation of more than $2{\cdot}10^5$ channels. As absorber material stainless steel is foreseen for cost reason. In the scintillating tiles solution the energy is extracted from the signal amplitude.
For the digital calorimeter, the information of the energy deposited per cell is not

used, and the total energy of a shower is obtained by the hit multiplicity. So a high segmentation is recommended to reduce the hit occupancy per cell to a minimum.

2.2.3 Particle Flow Algorithm

Many signatures of new physics are expected to produce hadronic final states. The hadronic final states are seen in the detector as multi particle bunches, called jets. They are best analysed using the particle flow concept. The particle flow concept [10] is based on the idea of increasing the precision of the four-momentum reconstruction of a jet, by combining the response of all detector components. The charged particles momentum is measured with high precision in the tracking device. The energy of photons will be measured best in the ECAL. The HCAL has to be optimised to measure the energy of neutral particles.
Especially in jets the tracks of charged particles are close to tracks of neutral particles. To separate the showering particles the spatial event topology has to be extracted. This can be done best with a fine granular reconstruction of the shower development. For particle flow a high granularity is mandatory.
For the reconstruction of a jet four-momentum, the shower clusters coming from shower generated particles, have to be connected to the incoming particle. For charged particles a shower can be connected to a track.
The first step in the identification of the shower is done on the level of cells. The cells are assigned to a cell class to form an initial cluster. The cluster shape is then iterated by reassigning cells to clusters. Subsequently clusters are merged to form the final shower. Once the full shower is reconstructed, it can be classified on the basis of its topology. The cell classes and algorithms depend on the used calorimeter type. In a digital calorimeter only the information of cell hits is stored. Clusters can be identified from hit density.
In a more classical analog calorimeter, where the signal amplitude is correlated to the deposited energy, the signal amplitude is used for classification.
As an example, three types of shower ingredients can be assigned: 1. MIP signals where no shower is developing, 2. signals with hadronic deposition and 3. electromagnetic shower signals as shown by the three possible separation lines in figure 2.2(a). The clustering algorithm groups the cells into clusters, calculating the origin direction as shown in 2.2(b). A shower algorithm combines the clusters and the track like signals to a complete shower. In this way the energy information of the calorimeter is obtained. For charged particles, the shower is substituted by the more precise momentum measurement of the tracking device.

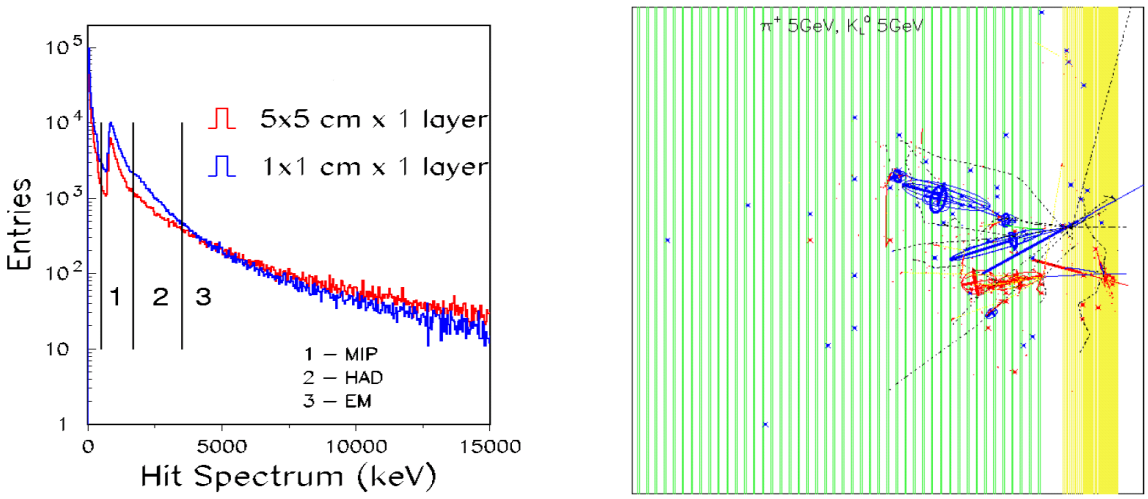

(a) (b)

Figure 2.2: (a) Example of a classification of a cell by deposited energy. (b) Example of particle flow reconstruction of a π^+ and a K^0_L. The upper particle is a K^0_L, the lower a π^+ both generating a hadronic shower. Both from [11]

2.3 Magnet and Muon Chamber

The proposed magnet in the TESLA TDR is a superconducting solenoid which produces a magnetic field of 4T. Such a high magnetic field is required by the tracking system for high momentum resolution and for the particle flow approach, scince it spreads the particles in the jet from each other. For TESLA, the magnetic flux return yoke also acts as a tail catcher to stop hadronic shower tails that developed in the outer region of the HCAL.
The Muon detecting chambers are also integrated into the return yoke for the magnetic flux.

Chapter 3

Physics in a Calorimeter

For the work presented in this thesis it is relevant to discuss in detail the physics processes of light production and light detection taking place in a calorimeter. The ways a particle interacts with matter leaving a detectable light signature are addressed in section 3.1. The distinction between electromagnetic and hadronic interaction in a calorimeter are treated in sections 3.2 and 3.3 respectively. In Section 3.4 a general description of a sampling calorimeter is given and the energy resolution discussed. The last section of this chapter is devoted to light detection. Various types of light detectors are described which are relevant for the studies presented.

3.1 Particle Interaction with Matter

The measurement of energy of a particle in a calorimeter is possible due to interaction of the particle with the material of the calorimeter. A particle passing through matter interacts with its electrons and nucleons loosing kinetic energy. The interaction with matter can be electromagnetic as for leptons, photons and charged hadrons or strong for charged and neutral hadrons and only rarely weak.
The mean energy loss $\frac{dE}{dx}$ (or stopping power $\frac{dE}{\rho dx}$) due to ionisation is given by the Bethe-Bloch formula. In figure 3.1 the stopping power for a muon in Cu is presented as a function of the muon momentum. The ionisation energy loss decreases until reaching a minimum around $\beta\gamma = 3$ to 4 (minimum ionisation), then starts to rise again. The numerical value of the minimum ionisation, or minimum energy loss is $\frac{dE}{\rho dx}$ = 2 MeV cm^2/g. For high relativistic energies radiation losses due to bremsstrahlung are dominating. The energy at which the ionisation losses start to dominate over radiation losses is called critical energy E_{crit}. The ionisation is a statistical process. The distribution of deposited energy is approximately Gaussian for thick absorber materials, but develops asymmetry and a tail towards high energies for decreasing thickness; it becomes a Landau distribution for very thin absorber materials.
Charged particles with energies below E_{crit} but higher than $\beta\gamma$=1 are called Minimum

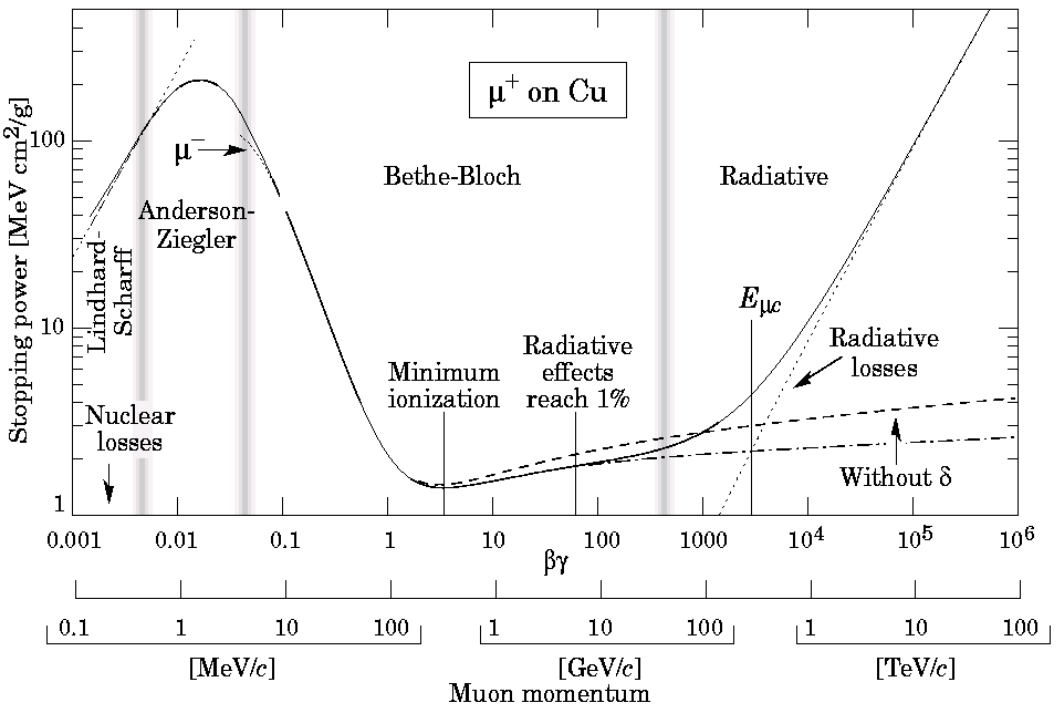

Figure 3.1: Stopping power for muons in copper [23].

Ionising Particles (MIP). These particles loose very little energy when traversing a medium. Radiative losses are only relevant for electrons due to the small mass.
An empirical definition of the critical energy [2] is given as

$$E_{\text{crit}} = \frac{610\text{MeV}}{Z + 1.24} \tag{3.1}$$

The ionisation energy loss is to a good approximation proportional to the electron density in the medium and therefore to Z, the medium atomic number. The value of E_{crit} is smaller the denser (high Z) the material is. So in a high density material radiative processes are initiated by low energy particles, yielding a better energy resolution (see section 3.4). Calorimeters with good resolution should be built of materials with high Z.
Low energy photons interact with matter mainly via photo effect with the electrons of the medium. At high energies pair production becomes the dominant process for photons.
The average energy loss of hadrons is mainly due to strong interactions, which eventually even destroy the particle producing secondary hadrons, mostly π, p ,n [2]. Nevertheless, electromagnetic energy loss of hadrons is important, because the mean free path for strong interactions is large. If the hadrons are neutral, they only can interact strongly.

3.2 Electromagnetic Showers

High energy leptons or photons can initiate electromagnetic showers via bremsstrahlung or pair production processes. The secondary electrons, positrons and photons produced will also undergo the same processes in a production cascade (see fig. 3.2). This cascade will develop until the radiation energy is below the energy of pair production. At this stage the shower intensity reaches its maximum. Afterwards only ionisation and Compton scattering will occur and the shower decays slowly.
An electromagnetic shower has two components, one dominated by the radiation, which is mostly directed in forward region. The other component is created by diffusing electrons from ionisation processes and is, therefore, transversally broader.

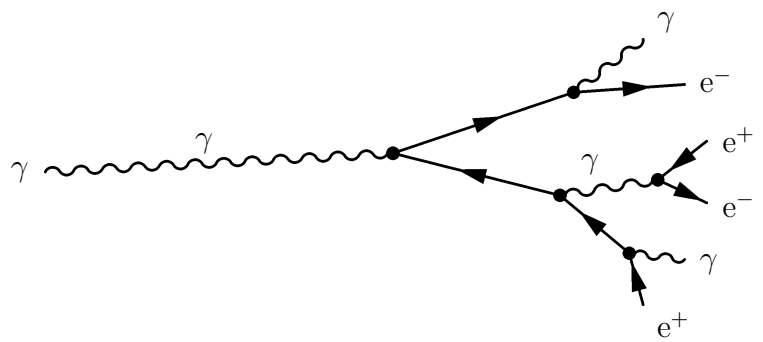

Figure 3.2: A simple electromagnetic shower induced by a photon.

The electromagnetic shower shape scales in the longitudinal direction approximately with the radiation length X_0, and in the lateral direction with the Moliere radius. The radiation length is a scaling variable for the probability of occurrence of bremsstrahlung or pair production, and for the variance of the angle of multiple scattering. The radiation length is given by:

$$\frac{1}{X_0} = \frac{4\alpha N_A Z(Z+1) r_e^2 ln(183 Z^{-\frac{1}{3}})}{A} \tag{3.2}$$

where $r_e^2 = 2.818 \times 10^{-13}$cm is the effective electron radius, N_A the Avogadro number and α the fine structure constant.
The average energy loss for bremsstrahlung is expressed in terms of X_0 as $-\frac{dE}{dx} = \frac{E}{X_0}$. The probability for an electron positron pair to be created by a high energy photon is 63% in $\frac{7}{9}X_0$. Since X_0 is inversely proportional to Z^2, it can be noted that for the same thickness of material traversed a particle looses more energy in a dense material than in a material with small Z or large X_0.

The Moliere Radius is the material dependent average transverse size of an electromagnetic shower. It is given by the empirical expression [2]:

$$R_{\text{Moliere}} = 0.0265 X_0 (Z + 1.2). \tag{3.3}$$

A dense material has a smaller R_{Moliere} than a light one and therefore the electromagnetic shower is more compact in the transverse direction.
The depth of a calorimeter is depending on the radiation length X_0 of its absorber material. The more radiation lengths the calorimeter covers, the less energy leakage it has. So for the same length, a calorimeter with a short radiation length material has less leakage than one exploiting a material with higher X_0. The granularity of a calorimeter should be the size of the Moliere Radius. Finer granularity would give no more information to distinguish between two particle showers.

3.3 Hadronic Showers

The hadronic showering process is dominated by a succession of inelastic hadronic interactions. At high energy, these are characterised by multi particle production and particle emission originating from decays of excited hadrons. While charged hadrons can lose their energy by ionisation (like electrons) the neutral particles will lose energy only by strong interaction. The scaling variable introduced to describe hadronic multiplication processes is the nuclear interaction length λ_{I}, which is energy independent and it represents the mean free path of a particle before undergoing inelastic scattering.
Secondary particles generated by strong interaction are mostly charged and neutral pions. Neutral pions decay electromagnetically into two photons ($\pi \rightarrow \gamma\gamma$). Therefore, hadron showers generally contain a component that behaves electromagnetically.
$\pi^{\pm}$ have a much longer lifetime than the π^0. Thus most $\pi^{\pm}$ interact strong generating separated shower clusters. They rarely decay into muons before being stopped or undergoing further interactions. The fraction of the initial hadron energy converted into π^0 varies strongly from event to event. But on average the electromagnetic fraction is ([2]):

$$f_{\text{em}} = 1 - (\frac{E}{E_0})^{-0.2} \tag{3.4}$$

where E_0 corresponds to the average energy needed for the production of one pion and depends on the Z of the absorber material.
The hadronic shower shape is scaled with the calorimeter's interaction length. Due to the production of secondary showers, the hadronic showers have a widely fluctuating shape.
Discrimination between electromagnetic and hadronic showers is a major criterion for a calorimeter; it is, therefore, important to contain electromagnetic showers over a short distance, without initiating too many hadronic showers. The critical quantity to

minimise is the ratio X_0/λ_I , which is approximately proportional to $Z^{1.3}$ [12]; hence the use of high-Z materials like lead, tungsten or uranium for electromagnetic calorimeters.

3.4 Sampling Calorimeter

The calorimeter is a composite detector using total absorption of particles to measure the energy and position of incident particles or jets. In the process of absorption showers are generated by cascades of interactions. A calorimeter can be built in different ways, as a homogeneous or a heterogeneous (sampling) calorimeter. In homogeneous calorimeters the functions of passive particle absorption and active signal generation are combined in a single material. If the signal is visible light, a transparent material has to be used to allow light collection.
In sampling calorimeters these two functions are separated. This allows optimal choice of absorber materials and a certain freedom in signal treatment. Heterogeneous calorimeters are mostly built as sandwich structures, alternating sheets of heavy-material absorber (e.g. lead, iron, uranium) with layers of active material (e.g. liquid or solid scintillators, Cherenkov or proportional counters). Only the fraction of the shower energy absorbed in the active material is measured.
The signal produced by a shower inside one layer of active material is integrated. If the information of the shower development is needed, as required for the particle flow technique described in section 2.2.3, the active material must be divided into small size cells. This can be realized easier in a sampling calorimeter than in homogeneous calorimeters; particularly in the longitudinal direction.
For practical uses it is desirable for the shower to be fully contained inside the calorimeter. Transparent materials have generally low-Z, or large X_0. In a sampling calorimeter transparent low-Z material is alternated with high-Z absorption material, yielding a more compact structure for the same shower containment than a homogeneous calorimeter.

3.5 Energy Resolution

The performance of a calorimeter is generally expressed in terms of its energy resolution. The energy resolution is limited by statistical fluctuations inherent in the development of showers, and by instrumental and calibration limits. The basic phenomena in showers are statistical processes, hence the intrinsic limiting accuracy, expressed as a fraction of total energy, improves with increasing energy as:

$$(\sigma/E)_{\text{fluct}} \propto 1/\sqrt{E} \tag{3.5}$$

Over much of the useful range of calorimeters, this term dominates the energy resolution. For sampling calorimeters this term is dominated by sampling fluctuations and

this limits its the energy resolution. A second component is due to instrumental effects, being rather energy-independent (noise), its relative contribution decreases with E:

$$(\sigma/E)_{\text{inst}} \propto 1/E \tag{3.6}$$

this component may limit the low-energy performance of calorimeters. A third component is due to calibration errors, non-uniformities and non-linearities in photomultipliers, proportional counters, ADCs, etc. This contribution scales with the energy:

$$(\sigma/E)_{\text{sys}} \propto \text{const} \tag{3.7}$$

This component sets the limit for the performance at very high energies. The different terms are uncorrelated, thus the total energy resolution is calculated as:

$$\frac{\sigma_E}{E} = \frac{a}{\sqrt{E[\text{GeV}]}} \oplus b \oplus \frac{c}{E} = \sqrt{\left(\frac{a}{\sqrt{E[\text{GeV}]}}\right)^2 + b^2 + \left(\frac{c}{E}\right)^2} \tag{3.8}$$

The term $a/\sqrt{E}$ is referred to as the stochastic term, b is the constant term and c/E the noise term. The determination of these values is necessary to quantify the calorimeter performance.

3.6 Photodetectors

If the calorimeter active material is based on photon production, like a scintillator, the readout can be done with photodetectors. These are devices to convert light into an electric signal. A well established type of photodetector for calorimetric purposes are photomultiplier tubes, which work exploiting the photoelectric effect [20]. Another technique for light detection is the use of semiconductor devices, which exploit the photovoltaic effect to convert photons into electrons.
The photoelectric effect is observed above a material-dependent wavelength threshold. An electron is released from the metal surface. The photovoltaic effect is observed when light is falling on a diode. The photons create electron hole pairs and causes a voltage to develop across the device, leading to a current in the forward bias voltage direction.
Two types of silicon based photodetectors are investigated for the present work:
Avalanche Photo Diodes (APD) and Silicon Photomultipliers (SiPM). The principle of operation of these photodiodes is similar to that of a standard p-n junction, shown in figure 3.3. If a photon penetrates the detector it produces electron-hole pairs, the number being proportional to the energy loss. An externally applied voltage generates a high electric field in the barrier layer which separates the pairs before they recombine; electrons drift towards the anode, holes to the cathode. The drifting of the charges produces a current pulse on the electrode, whose integral equals the total charge generated by the incident particle (i.e. is a measure of the deposited energy), if the diode

is operated with no intrinsic gain.
Silicon detectors are asymmetric p-n junctions; to work as a detector, the diode is reverse-biased by applying a positive voltage on the rear ohmic contact, a metal deposited on the n side. At full depletion, the electric field is a maximum in the junction

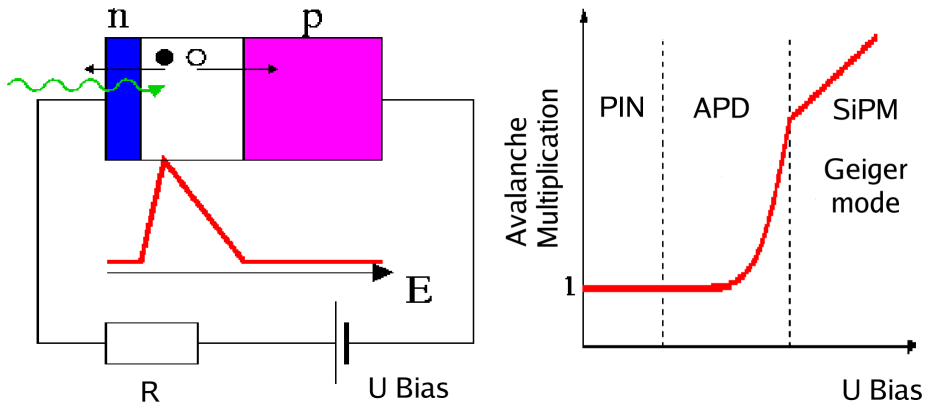

Figure 3.3: a) Principle scheme for APDs and SiPMs. b) Voltage dependence of the gain.

and decreases to zero at the ohmic contact. In order to avoid losses in charge collection, the silicon detectors are operated above the proportional voltage (below break-down voltage).
The intrinsic energy resolution is related to the low energy threshold: only 3.6 eV are necessary to produce an electron-hole pair, a low value compared to the ionisation energy in a gas (30 eV) or the approximately 300 eV necessary to extract an electron from a photocathode coupled to a plastic scintillator.
Due to the strong electric field, secondary electron-hole pairs are produced and an avalanche is started. The avalanche intensity, or multiplication, depends on the bias voltage, as shown in fig. 3.3.
In order to compare various photodetectors some physical quantities are introduced in the following. The probability for a photon hitting the photodetector to extract the primary photoelectron is called quantum efficiency (QE). The number of secondary electrons generated as a cascade from the primary photoelectron gives the gain, or avalanche multiplicity of a photodetector. The sensitivity describes how many photoelectrons are needed to initiate a shower. The dark rate gives the amount of signals induced by spontaneous electron emission by temperature and other non signal photon effects. The dynamic range is the range in which the response of a photodetector is proportional to the light input.
A comparison of the main photodetector properties is given in table 3.1 for the used photo tube and two types of photodiodes, SiPM and APD.

Property	PMT	APD	SiPM
gain	10^5	10^2	10^6
bias voltage	800 V	400 V	60 V
Quantum eff. @ 500 nm	20%	75%	15%
sensitivity	1 - 2 p.e.	50 p.e.	1 p.e.
dynamic range	10^4	10^4	10^3
Dark Rate	few 10 kHz	few 10 kHz	few MHz
Size of active area	$4.5\times4.5\,mm^2$	$3\times3\,mm^2$	$1\times1\,mm^2$

Table 3.1: Comparison of basic properties of the photodetectors PMT, APD, SiPM used in these studies.

3.6.1 Vacuum Photo Tubes

A standard light detector is the photomultiplier tube. Since this device is well established in light readout for calorimeters we use photomultipliers for comparison with the new photodetectors. The primary conversion of photons into electrons is achieved by a photocathode using the photoelectric effect [20]. Electrons are emitted if the photon energy is sufficient to detach an electron from the cathode material.
Multiplication is done by collision with a series of dynodes. A high voltage is applied to the dynodes (see fig. 3.4) and a high electric field accelerates the electrons to each dynode. Typically 2 - 3 electrons are produced per colliding electron. As a result an avalanche shower of electrons is created.

A current which is decoupled at the anode plate is created. The gain is dominated

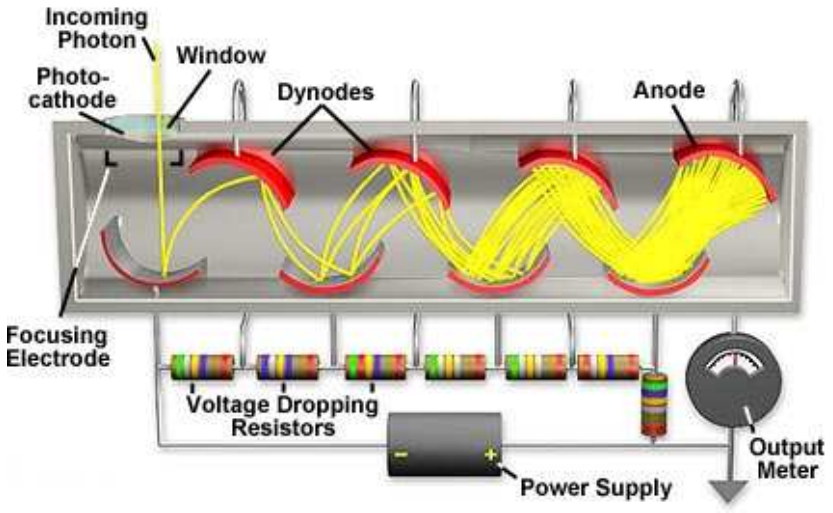

Figure 3.4: Working principle of a vacuum photo tube.

by the high electric fields. There is only a small temperature effect in gain of less than 1%/K [16]. A more detailed description is given in reference [19].
Photomultipliers are fast devices, the signal has a typical rise time of about 1 ns and 2 ns fall time [16]. Their gain can reach up to 10^6 depending on the applied voltage.
The photomultipliers used in this work are H8711 and H6568 Hamamatsu multi-anode photomultipliers with 16 channels. The typical operation voltage ranges between U=600 V and 1500 V. Single photoelectron peaks can be detected. The quantum efficiency is about 20% for peak sensitivity (wavelength λ_{peak}=420 nm). The noise is dominated by thermal electrons inside the multiplication tube. Noise is producing a dark current of less than 10 nA for a gain of 10^6. The linearity is given for signals up to 1 mA. Higher signals saturate the dynodes and the signal amplitude is no longer proportional to the number of primary photons.
When used in magnetic fields stronger than typical 500 mT, the photo tube signal is degenerated. Electrons in the multiplication cascade are deflected, they do not reach the dynodes and as a result the signal is reduced.

3.6.2 Avalanche Photo Diodes

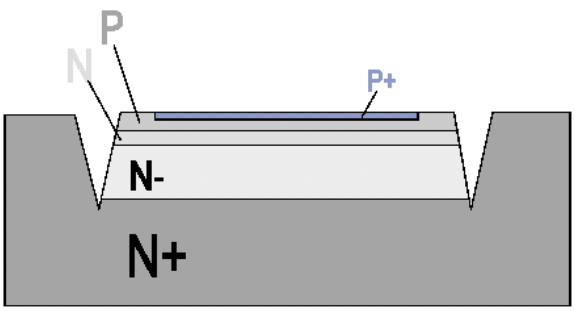

Figure 3.5: Sketch of an APD.

Avalanche Photo Diodes (APD) are silicon based photodetectors operated in avalanche mode. The applied bias voltage leads to an avalanche multiplication process for generating electron-hole pairs, which leads to high gain. The gain is strongly dependent on the applied voltage. The integral of the pulse signal collected for one event is proportional to the total number of incoming photons.
These devices are commercially available from many manufacturers and are fabricated with different solid state structures. They are commonly used in fibre optic communications and in some high energy physics detectors like CMS [25].
APDs are operated typically with a bias voltage of 100 - 500 V [15] which correspond to a gain of 1 - 10^4. The gain is also strongly temperature dependent. As an example voltage and temperature dependences of a Hamamatsu type APD are shown in figure 3.6. APDs have a dynamic range of 10^4 and a high quantum efficiency of about 80%

for green light. The range of wavelengths where the quantum efficiency is at maximum can be set by the depth of the doped layers which also affects the capacitance. In the above scheme the low negative doped layer (N-) is increasing the sensitive area, which is important for long wavelength sensitivity. The low doping reduces the capacitance increase to a minimum. High voltage breakdown at the edges can be prevented by a groove etched into the layer structure.

As the gain is decreasing with increasing temperature, the signal to noise decreases.

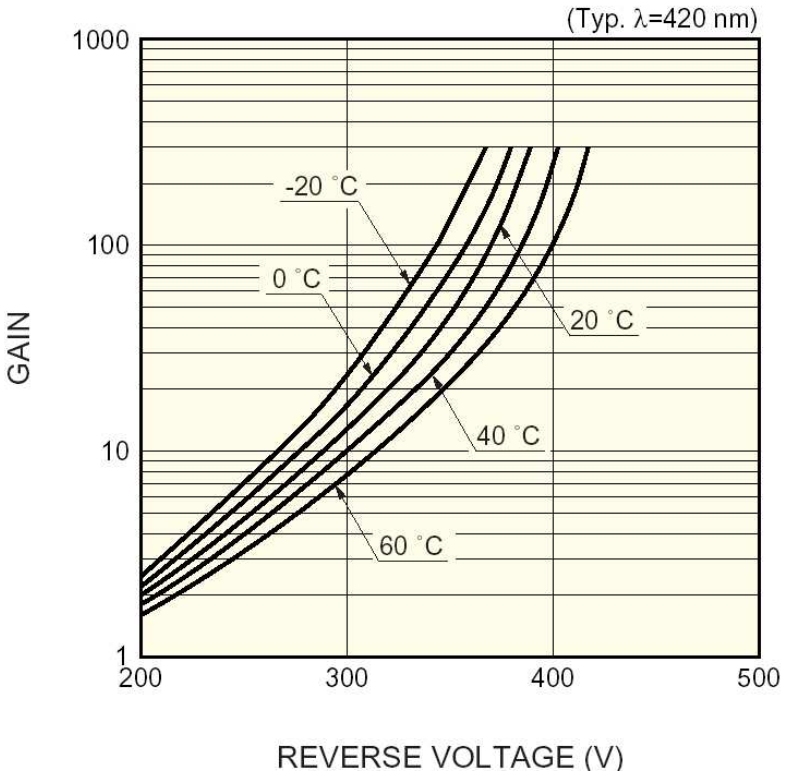

Figure 3.6: Temperature and voltage dependence for S8664-55 APDs from Hamamatsu.

Thus the best signal to noise ratio is at low temperatures.
In addition, the avalanche process generates current fluctuations, and the APD performance is degraded by an excess noise factor compared to a PIN diode of gain 1. The excess noise factor is defined as:

$$F = k \cdot M + (2 - \frac{1}{M}) \cdot (1 - k) \tag{3.9}$$

where k is the ratio of ionisation coefficients for holes and electrons and M the gain. The excess noise factor for CMS type APDs is ≈ 2 for a gain of 50. The excess noise factor for SiPM is ≈ 1. The total noise current is given by:

$$I_{\text{noise}} = (2e \cdot (I_{\text{DS}} + I_{\text{DB}} \cdot M^2 \cdot F)B)^{\frac{1}{2}} \tag{3.10}$$

where I_{DS} is the dark current on the surface, I_{DB} the bulk leakage dark current and B the system frequency bandwidth. The dark currents are noise induced currents. While the surface dark current is independent of the gain the bulk current is not.
In the absence of other noise sources, an APD provides a signal to noise which is $F^{0.5}$ worse than a PIN detector with the same quantum efficiency and dark current. An APD however, can produce a better S/N ratio than a PIN diode, where the gain increases the signal without affecting the system noise.
The low gain of APDs leads to the requirement of a preamplifier. The preamplification of the electronic signal introduces additional noise which has to be kept minimal by the accurate optimisation of the preamplifier characteristics.
Typical APDs on the market have a capacity of 1 to 500 pF. The signal length is proportional to the internal capacitance. For the purpose of fast readout a small capacity is needed. Our APDs are similar to that used by CMS [25]. They have ≈ 20 pF at 400 V bias voltage as shown in section 6.1.1.

3.6.3 Silicon Photomultiplier

The Silicon Photomultiplier (SiPM) is a semiconductor based device operated in limited Geiger mode. In this mode the amplitude of the avalanche is not proportional to the number of primary photoelectrons generated by the incident photons. To stop the avalanche, the bias voltage has to be reduced below breakdown voltage. This is achieved by putting in series a resistor of 10 kΩ. The avalanche induced current reduces the bias voltage.

To get a signal proportional to the number of produced photoelectrons, the silicon

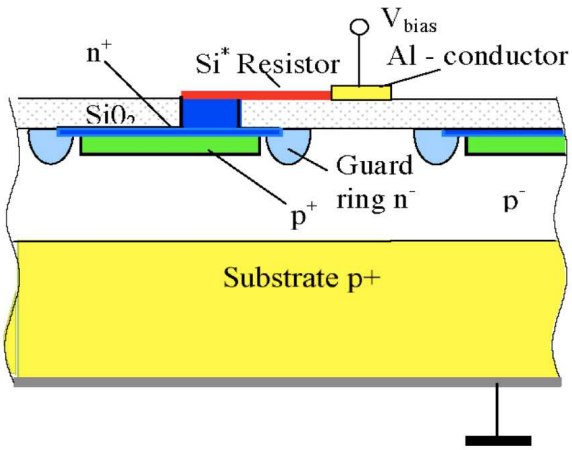

Figure 3.7: Sketch of a SiPM structure.

is segmented into small size pixels (figure 3.7). The SiPM used in MiniCal tests have 1024 pixels. Each pixel behaves as a diode in Geiger mode producing equal amplitude

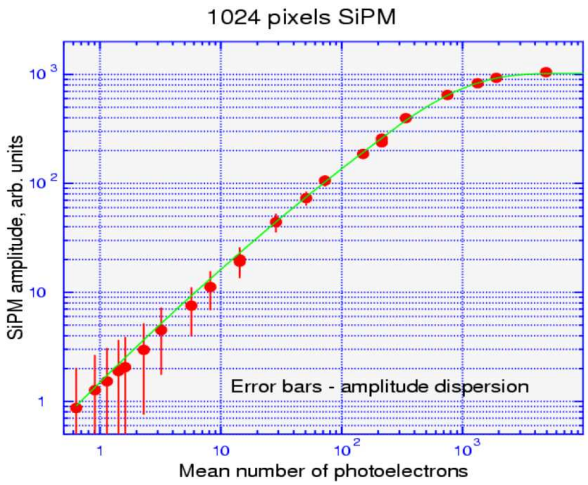

Figure 3.8: Saturation curve for a SiPM.

signal responses to an input photon. To avoid electron crosstalk between pixels, each pixel has a guarding ring to shield it from the field of neighbouring pixels.
The limited number of pixels in a SiPM determines its nonlinear response function shown in figure 3.8. The limit depends on the number of pixels.

Chapter 4

MiniCal Calorimeter Prototype Setup

A small size prototype called MiniCal has been built by a subgroup of the CALICE collaboration[1]. The purposes of this prototype are to gain experience in the construction and operation, and to establish new technologies needed for a large prototype for physics studies, as proposed by the CALICE [13] collaboration.
In the MiniCal the readout of several channels with various photodetectors is investigated. The design of the tile fibre system is optimised. The long term signal stability and the reproducibility of calibration is studied.

4.1 Main Structure

The MiniCal shown in figure 4.1 is built of 28 layers of stainless steel absorber plates. Each plate has a thickness of 20 mm. The plates are stacked with a gap of 10 mm where cassette plates with scintillator material can be inserted. The structure is contained in a box of $0.5 \times 0.5 \times 1\,\mathrm{m}^3$ of sheet metal. So the box is closed light tight and electrically shielded. The box is surrounded by a support structure allowing mechanical movement with a crane to switch from horizontal beam operation to vertical cosmic muons calibration. On one side of the MiniCal box three window plates are mounted holding photodetectors and cable connections. A fan is installed inside the MiniCal to improve temperature homogeneity. The temperature is monitored by 3 temperature sensors read out independent from the data taking by a slow control system.

[1]The institute members are: DESY, Univ. of Hamburg, ITEP, LPI, MEPHI, Univ. Prague

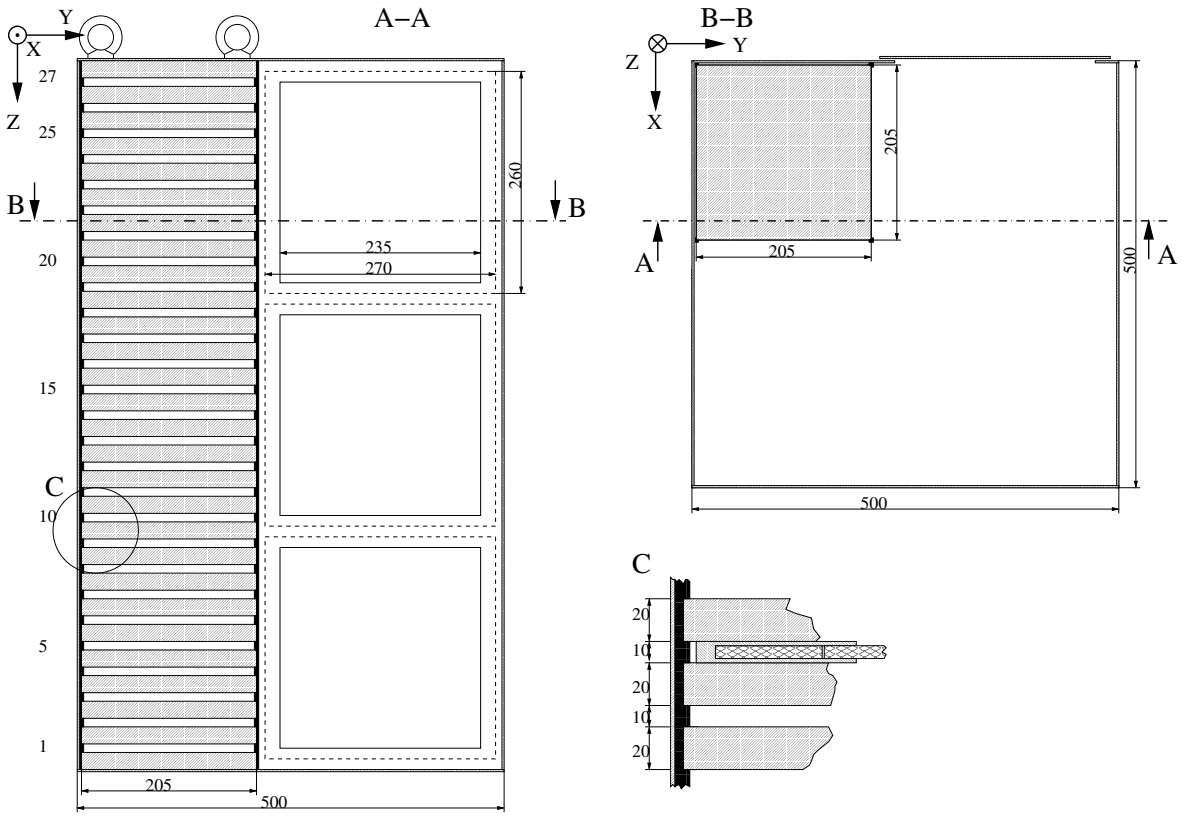

Figure 4.1: Structure design of the hadron calorimeter prototype (MiniCal). Shown is the side view as oriented for cosmics data taking and the 3 windows for photodetectors and cable connections on the right. The top view is shown on the right side. The stainless steel absorber plates are shown in detail marked as C.

4.2 Cassettes

The scintillating material is inserted into the MiniCal structure in a cassette of 9.5 mm height. Each box called cassette holds 3×3 scintillating tiles of $5\times5\,\mathrm{cm}^2$. The tiles have a thickness of 5 mm. Thus, the active size is $15\times15\times0.5\,\mathrm{cm}^3$ in each cassette which is about 6.5 $R_{M,eff}$, the Moliere radius of the sandwich. Figure 4.2 shows a picture of one of the cassettes used in the MiniCal. This gives the prototype more flexibility, because of easy exchange of scintillation material and photodetectors.
The scintillating tiles are made of organic scintillating molecules in polystyrene by Bicron (BC408). Each tile has a circular groove in which a 60 cm wavelength shifting fibre is inserted as shown in figure 4.2. The wavelength shifting (WLS) fibre is a double clad type (Y11, 300 ppm) from Kuraray. One polished end of the WLS fibre is connected outside of the cassette on a photodetector. The other end is covered with reflector material to minimise light losses. Each scintillator tile is wrapped with

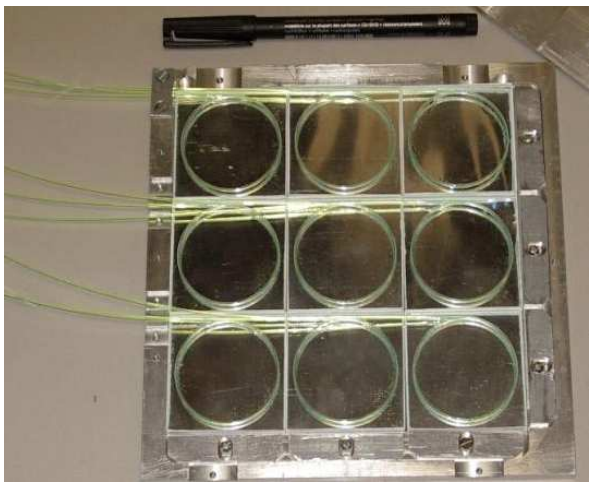

Figure 4.2: One MiniCal cassette containing 9 scintillator tiles with WLS readout.

reflecting foil (VN2000 superradiant from 3M).

4.3 Readout

The Readout of the calorimeter is done from optical to the electrical signal processing. The optical readout path is shown in figure 4.4. When particles traverse the active material, the scintillator is activated. Scintillation light of about 430 nm (see spectrum fig. 4.3(a)) is emitted. The blue scintillator light is collected from the WLS-fibre embedded into the tile. The blue light is here absorbed by the organic scintillator and re-emitted as green light with a peak wavelength of λ=500 nm as shown in figure 4.3(b). The WLS-fibre then acts as light guide transporting the green light to the

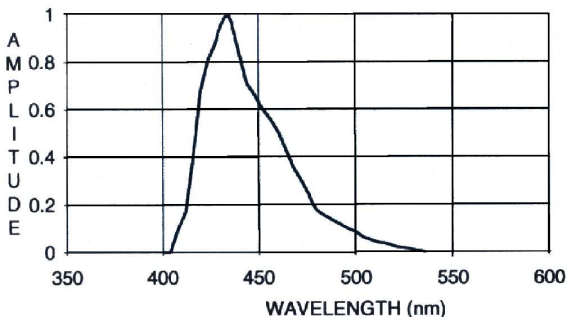

(a)

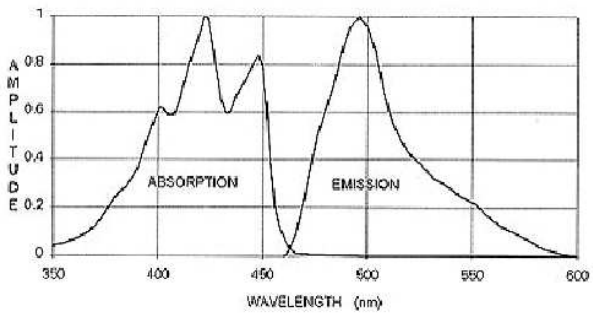

(b)

Figure 4.3: (a) The emission spectrum of the used scintillator from Bicron. The main emission is at 430 nm. (b) The absorption and the emission spectrum of the WLS fibre.

photodetector. The photodetector converts the light to an electrical signal. Usually photodetectors are optimised to cover the green light range.
We have equipped the MiniCal with 12 cassettes covering $14\,X_0$. As each cassette has 9 scintillation tiles, 108 channels are read out. To reduce the number of Photodetectors needed, only the central tiles are read out independently. The surrounding tiles are gathered in groups of three to build a cell readout by one photodetector. Thus, there are 4 cells in depth. This leads to a required readout of 44 channels. Having only 33 APDs available, we have to leave three of the corners not equipped for the APD tests. The side leakage is supposed to be smaller than 10% as explained in section 6.2.3.
The WLS-fibres are connected to the APD using masks with four holes to hold four fibres in front of the $3\times3\,mm^2$ active area of the APDs. Three WLS fibres and one clear LED monitoring fibre are connected to the APDs for the surrounding tile readout. For the central tiles one WLS-fibre and one clear LED monitoring fibre is connected.

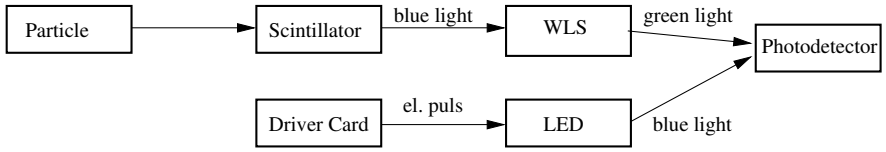

Figure 4.4: Optical way of a signal from the particle and from the LED pulse generator to the photodetector.

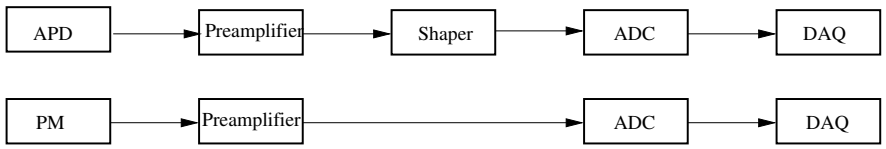

Figure 4.5: Logical way of a signal from photodetectors to the data acquisition.

The photodetector signals are shown in figure 4.6. The photomultiplier signal length is dominated by the decay time of the scintillator tile and the WLS-fibre.

The analogue signal output of the photodetectors is digitised (see figure 4.5) in an Analog to Digital Converter (ADC) module. We used CAMAC[2] modules from LeCroy No. 2249A and No. 2259B. The No.2249A ADC modules are charge sensitive modules with a range of 10 bits (1024 channels), the total charge of a signal is stored in a capacitor and converted into a digital number. The No. 2259B modules are voltage

[2]Computer Aided Measurement And Control, an interface defining a data bus technology for control and data transfer from electronic devices to computers.

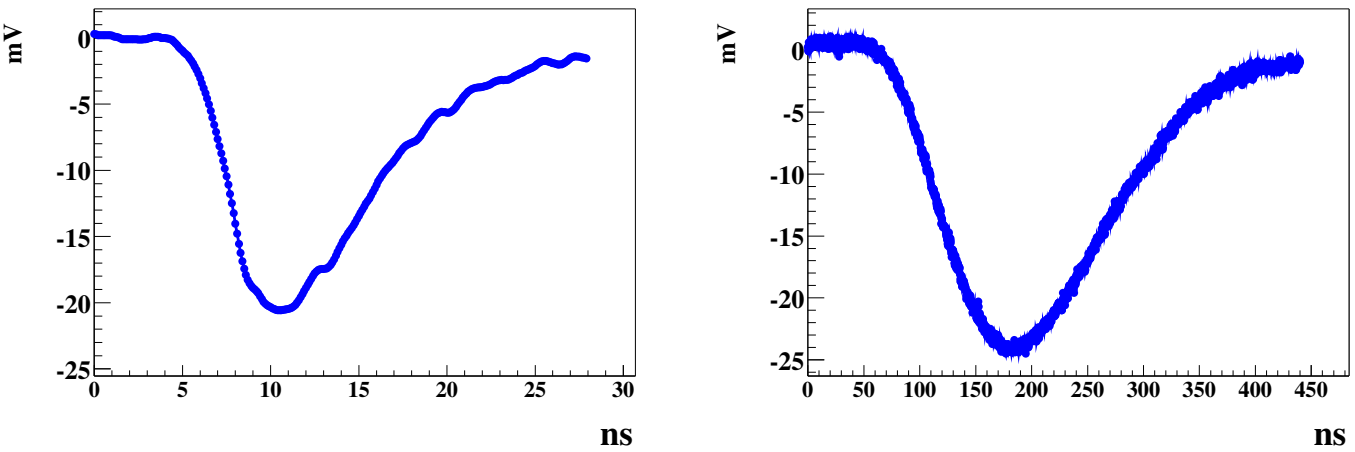

(a) (b)

Figure 4.6: (a) Signal of one tile for a MIP seen with a photomultiplier tube. The rise time is 5 ns, the fall time 20 ns. (b) Signal of one tile for a MIP seen with a APD and the Minsk preamplifier. This signal is processed with a shaper. The rise time is 120 ns, the fall time 250 ns.

sensitive and have a range of 11 bits (2048 channels). They are converting the peak voltage into a digital number. The data is stored in a ROOT[3] file for the analysis.

4.4 Preamplifier

The internal amplification of the APD of ≈ 100 is too low to feed the signals directly to an ADC module. An APD readout preamplifier is needed. Two types of single channel preamplifiers are used: A charge preamplifier made in Minsk and a voltage sensitive preamplifier made at the University of Prague.
A charge sensitive preamplifier is integrating over the signal current with a capacitive coupling. Thus it needs longer time than a voltage sensitive preamplifier. This preamplifier is using the maximum voltage. This is much faster but is more sensitive to pickup noise. Voltage amplifiers are often used in communication technics. A charge integrating amplifier is often used in high energy physics detectors due to lower noise sensitivity.
The measurements described in chapter 6.2 are performed with the Minsk charge sensitive preamplifier. The measurements are compared to data taken with the Prague preamplifier in the same section.
The charge sensitive Minsk preamplifier operates at 5 V and has a crosstalk of less

[3]ROOT is an object oriented data analysis framework provided by CERN members and based on C++ [29]

than 0.5%. The voltage sensitive Prague preamplifier is operated at 10 to 12 V, and has a crosstalk of less than 1%. It has a larger power consumption than the Minsk preamplifier. The APD voltage can be tuned within ±5% by trimmers [22].
For both preamplifiers nine channels where placed on one printed circuit board (PCB) that contains also the high voltage part. They both have shapers to form the output signal. The shaper of the Prague preamplifier uses the 2nd order Bessel approximation for low/high pass filters. The Prague preamplifier gives an output signal with a rise time of 40 ns and a width of 180 ns. The output signal at the Minsk preamplifier has a rise time of 120 ns and a fall time of 250 ns.

4.5 Beam Setup

For beam measurement we have access to a test beam produced by DESY II, a circular synchrotron accelerator used to feed DORIS and HERA. A bremsstrahlung beam is extracted from the DESY II electron beam by a carbon fibre target in the beam halo. The photons are converted to electron/positron pairs on a metal target. The revolution frequency of DESY II is 1 MHz and the bunch length about 30 ps.
A variable dipole magnet field is used to separate electrons from positrons and select the beam energy up to 6 GeV. The beam energy spread for the smallest collimator ranges from 6% at 1 GeV to 2% at 3-6 GeV [21].
The MiniCal is positioned on a movable stage at the testbeam 21 facility allowing horizontal and vertical precise positioning with respect to the beam. The photodetectors are connected to the readout via 25 m long 50 Ω cables. In front of the MiniCal a cross of two scintillator counters each 3 mm thick is installed. The coincidence of the

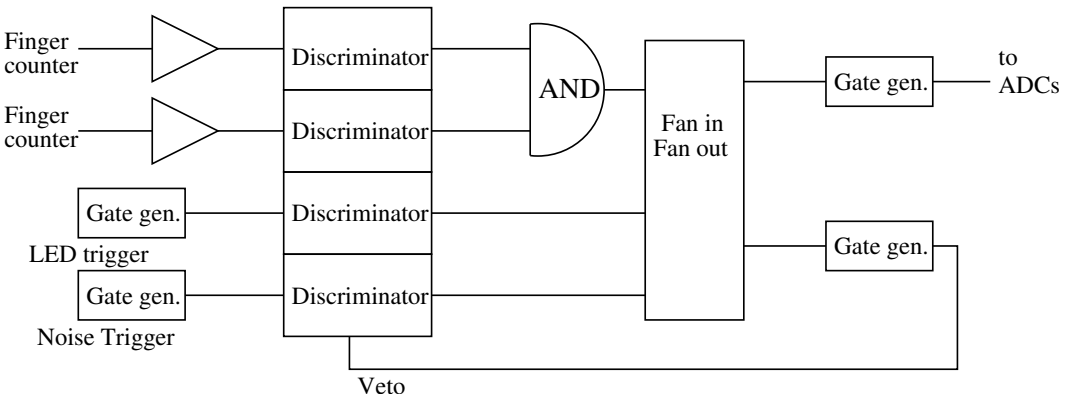

Figure 4.7: Scheme of the trigger system.

two discriminated signals of the finger counters provides the beam trigger. A sketch is shown in figure 4.7. Furthermore, an LED and a noise trigger are produced. The gate

signal is vetoed to prevent the DAQ from event pileup. Noise and LED triggers are given in between beam events with a frequency of 1 Hz to monitor the stability of the photodetectors and data acquisition. The monitoring is described in chapter 5.
The signal lengths are different for photomultipliers (PM) and APDs. The signal rise and fall time for a PM signal is ≈ 45 ns as shown in figure 4.6(a). A gate signal of 150 ns is used to readout the signal. The APD signal is ≈ 370 ns (figure 4.6(b)), as a shaper follows the preamplifier. Thus, a gate signal of 500 ns is used to collect the APD signal at the ADC.

Chapter 5

LED Monitoring System

One of the main goals of the MiniCal is to reach high stability and reproducibility of measurements. As the avalanche photodiode gain is primarily sensitive to high voltage and temperature changes, highest attention is payed to these effects. An LED monitoring system has been developed for this purpose based on the LED monitoring system concept that is successfully used in the SPACAL calorimeter for H1 [28]. The LED monitoring system is described in the next section. The temperature corrections of the data over short and long time periods are presented in section 5.2 and section 5.3 respectively.
The system response to a fixed input can change due to several effects. The most important effects are:

- The gain variation due to temperature dependence of the silicon based photodetectors (APD and SiPM) as described in sections 3.6.2 and 3.6.3.
- The gain variation generated by changes in the applied voltage produced by the power supplies.
- Aging effects of the scintillator material or the wavelength shifting fibre, which reduces the number of photons produced for a given input energy.
- Aging effects of the photodetectors, which reduce the quantum efficiency.

During the MiniCal operation no aging effect has been observed.
On daily or weekly basis the temperature variations are dominant, since the stability of the power supply from CAEN is better than 10^{-4}[30].
There are two standard ways of reducing the temperature effect in the data: temperature stabilisation of the photodetectors, or a correction for this effect after data acquisition. The temperature stabilisation is an expensive but known way of reducing the temperature effect. The possibility of temperature correction in the data is investigated. In this case the temperature changes of the APD signal is measured by

a temperature independent LED light pulse. Corrections to effects that are not correlated to the temperature are not investigated till now. This has to be done with cosmics data.

5.1 Setup

For monitoring the photodetectors a LED system is used. Blue LED light is distributed with 12 clear fibres per LED to several photodetectors as shown in figure 5.1. The fibres are 5 mm thick black coated fibres.

In the case of APD and photomultiplier monitoring, a mask is used to hold one

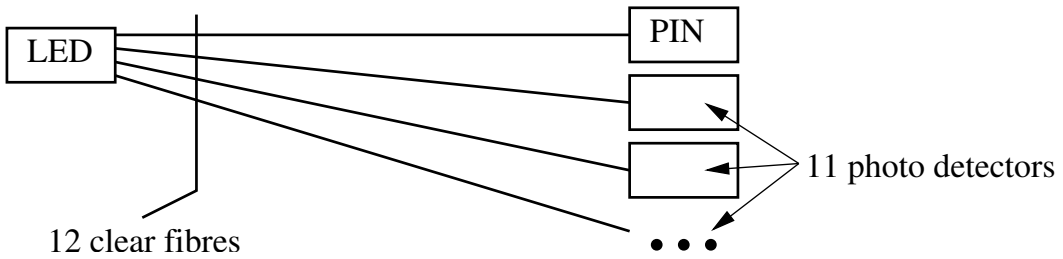

Figure 5.1: LED light distributing system with one clear fibre to a PIN diode and 11 clear fibres to photodetectors.

clear fibre from the LED together with up to three WLS fibres in front of the APD active area. Four LEDs (Osram HLMP-CB15) are used to feed a maximum of 44 photodetectors and four PIN[1] diodes from HP (SFA 203).
The PIN diode has been used to monitor possible light emission changes of the LED. A PIN diode is a semiconductor device operated with no internal amplification (gain=1). The electrical signal output is directly proportional to the incoming light intensity. The PIN diode signal is almost temperature independent in a wavelength range of 300 nm to 500 nm. The temperature dependence is 0.18 %/K.
The peak sensitivity is at 850 nm and the relative sensitivity at the used wavelength of 470 nm is about 30% shown in figure 5.2(b).
The preamplified PIN diode signal is read out together with signals from the other photodetectors.
The LED spectrum shows a maximum light output at a wavelength of about 470 nm. The spectrum is shown in figure 5.2(a). The LED driver board has been optimised for stable pulses of ≈15 ns with a repetition rate up to 1 kHz. This has been done by loading a capacitor parallel to the LED (figure 5.3(a)). The trigger signal opens the gate of the Field Effect Transistor (FET) and the capacitor is discharged via the LED. The light pulse produced by the LED driver circuit and observed with a fast PMT is

[1]PIN stands for the semiconductor doping scheme: Positive - Intrinsic - Negative doped

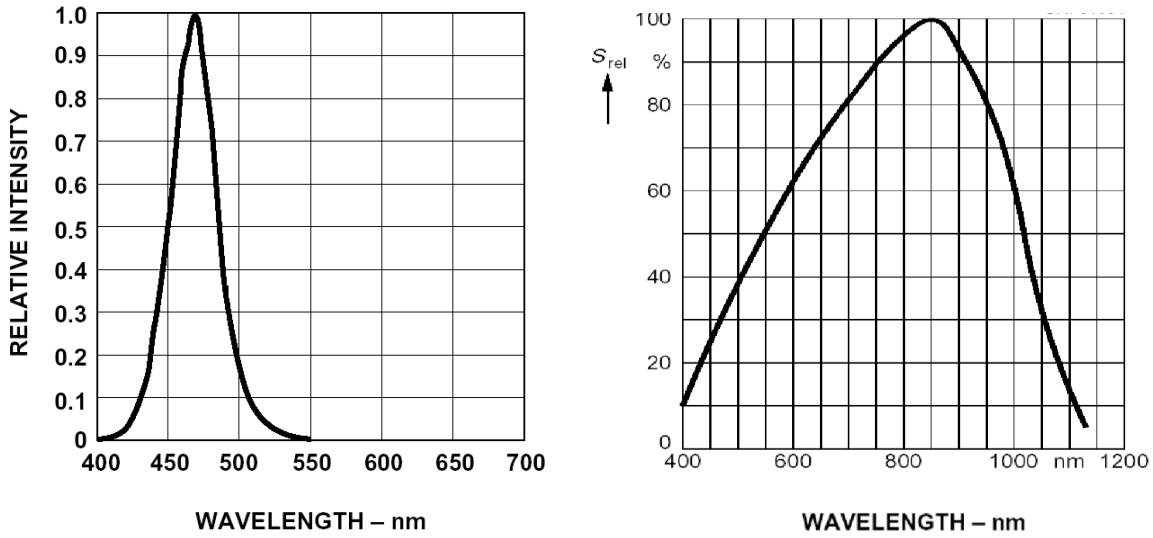

(a) (b)

Figure 5.2: (a) Spectrum of the LED light used in the monitoring system. (b) Relative spectral sensitivity of the used PIN diode.

shown in figure 5.3(b). The typical pulse has a rise time of 3 ns and a fall time of 12 ns. For measurements a frequency of 1 Hz has been used. As the LED signal shows a amplitude increase when warming up, the LEDs where operated before data taking. The effect can be seen in a longterm measurement in figure 5.6(b). The temperature

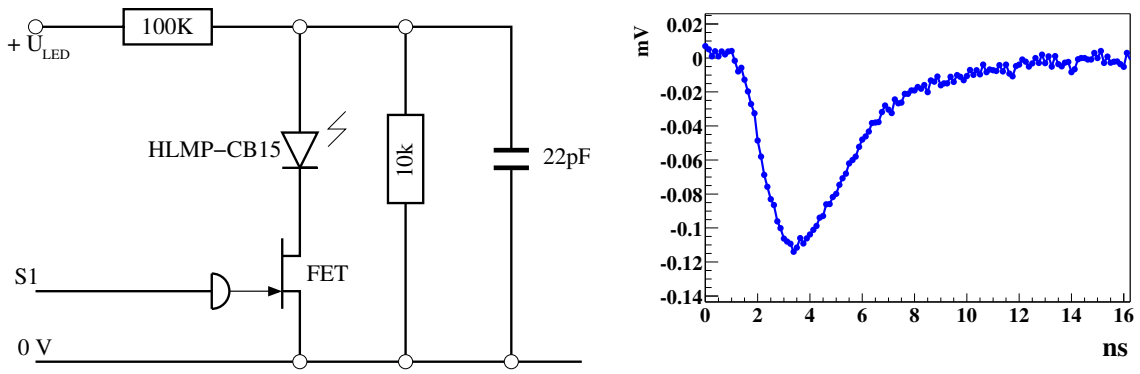

(a) (b)

Figure 5.3: (a) LED driver circuit diagram. (b) LED pulse produced with the LED driver circuit and observed with a fast PMT.

has been monitored by a separate slow control system based on a Labview program. The temperature has been measured by three sensors every 30 seconds.

5.2 Short Term Measurements

Typical energy and calibration scans (described in chapter 6) with the MiniCal are performed in short periods of approximately 2 h. An PIN diode signal of the LED light pulse has been recorded together with the signals from the photodetectors.
The LED monitoring system is used to check the APD gain changes for temperature shifts during one data acquisition period. The data is divided in several samples of short acquisition time and the signal average over each sample is calculated to reduce statistical fluctuations.
First the LED light emission temperature stability is checked by the PIN diode measurement. The PIN diode signal is stable within 1% as shown in figure 5.4 for two PIN diodes as representatives. The temperature variation during the entire period

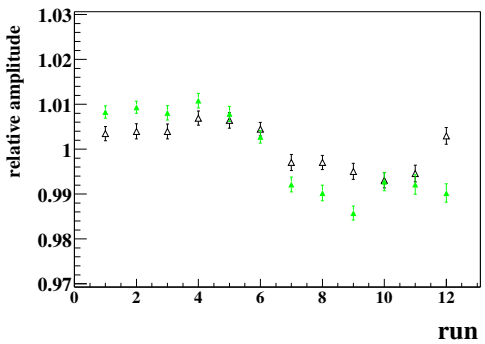

Figure 5.4: Relative amplitude of the LED signal recorded by 2 PIN diodes over 2 h of data taking.

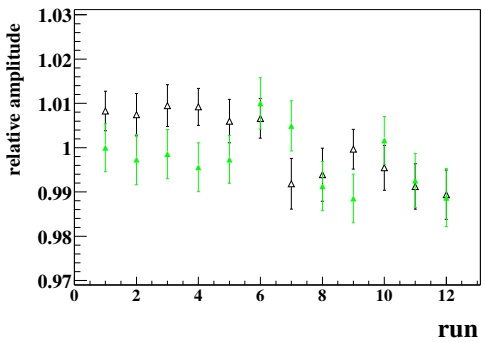

Figure 5.5: Relative amplitude of the LED signal recorded by 2 APDs over 2 h of data taking after PIN diode correction.

is less than 0.3 K. The LED response of the APD is then corrected by the PIN diode

response. This is done applying the following correction:

$$A'_{\mathrm{APD}} = A_{\mathrm{APD}} \frac{< A_{\mathrm{PIN}} >}{A_{\mathrm{PIN}}} \tag{5.1}$$

Figure 5.5 shows that a relative amplitude fluctuation of less than 1% in the APD response is observed. A larger error is expected from calibration. Thus no temperature corrections on short term measurements has been applied.

5.3 Long Term Measurements

Larger fluctuations can occur between two data taking periods. To study the precision of the LED monitoring system corrections for larger temperature variations, several long (exceeding 2 days) monitoring runs have been taken. The main source of fluctuation during this time is the temperature dependence of APD gain. In this long term runs the temperature is changing by about 1 degree as shown in fig. 5.6(a). The APD gain variation over the same period is given in figure 5.6(b). Each point in figure 5.6 is the average of 50 temperature measurements. The variation of the PIN diode signal shown in figure 5.6(c) and shows that the stability of the LED is better than 0.5% after an initial warm up time of about 1 hour.

There are two ways of compensation of temperature changes with this monitoring

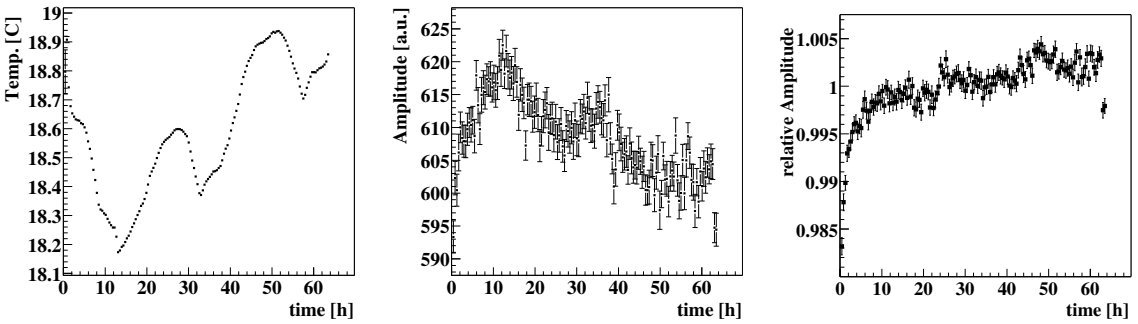

(a) (b) (c)

Figure 5.6: (a) Temperature shift in a 60 h run. (b) APD shift in gain seen with the LED signal for the same run. (c) PIN diode signal to monitor LED stability.

system.

The first method uses the fact that APD gain is anti-correlated to the temperature change. For small temperatures changes the temperature shift in APD gain can be approximated with a linear function. Thus the expected behaviour of the APD signal from LED is:

$$A(T, A_{\mathrm{PIN}}) = A'_0 \left(1 + \alpha \left(T - T_0\right)\right) \tag{5.2}$$

where A′ is the APD amplitude corrected for possible fluctuations of the LED signal as defined in 5.1. For APDs operated at gain of 120 it is expected to have a gain variation of ≈-4%/K. The APD data for a LED signal is plotted versus the temperature in figure 5.7(a). The fit parameters can be used to correct the APD signal for temperature variations. The slope shows the expected change in APD gain of α= -4.5%/K.
The expected LED signal seen by the APD for the given temperature shifts (from

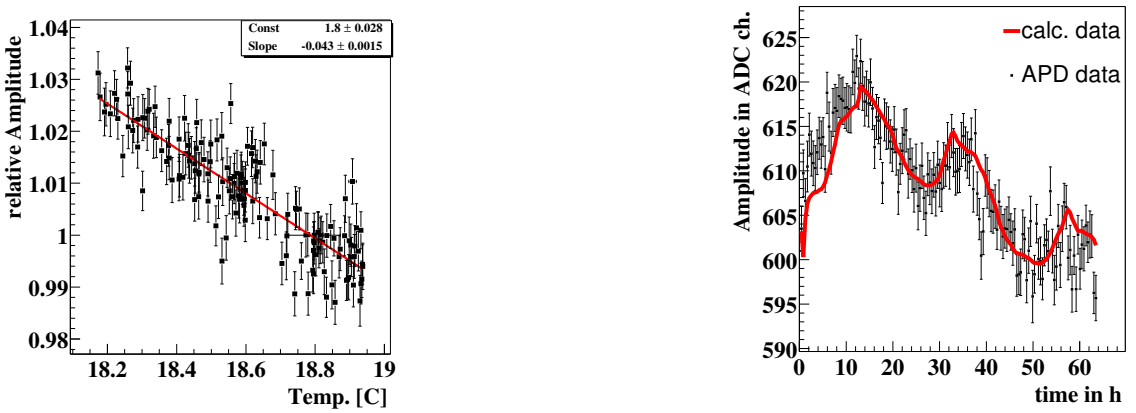

(a) (b)

Figure 5.7: (a) APD signal versus temperature. (b) APD signal and calculated curve for the given temperature.

temperature sensors) is shown in figure 5.7(b) together with the measured data. The good agreement between data and calculation demonstrates that the linear fit approximation is sufficiently good in this range of temperature changes.

This can also be seen from the improvement in the APD response of the LED light. The APD signal for LED light is smeared by the temperature changes as shown in figure 5.8(a). The APD signal is first corrected for possible LED shifts using the PIN diode signal. The correction has no significant impact on the signal distribution as it can be seen in figure 5.8(b). Secondly the temperature correction is applied and the signal distribution of figure 5.8(c) is obtained. The distribution has an initial spread of 0.01 and becomes Gaussian after applying the described corrections with a spread of 0.005. The remaining fluctuations are expected to be not temperature correlated.
With this method of correcting temperature shifts, the LED monitoring system is used to determine the APD gain change per Kelvin for one used gain. The corrections are then done on the basis of the temperature measurement.
The second method of compensation of changes uses the PIN corrected LED signal as reference. No temperature measurement is used. The shift of the APD response to the LED signal is expected to indicate the APD gain changes. This method is independent of the used gain or linear approximations. This method can be verified with cosmic

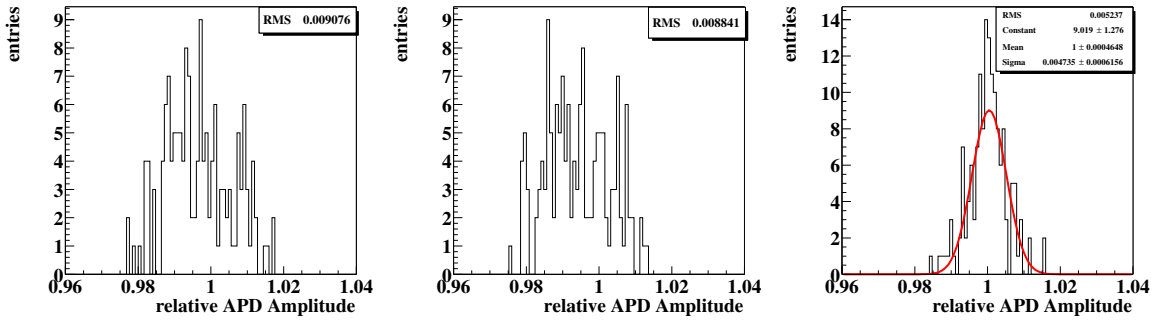

(a) (b) (c)

Figure 5.8: (a) APD signal distribution for LED light without temperature correction. (b) APD signal corrected for LED emission changes. (c) APD signal after correcting for temperature fluctuations.

muon data. The width of the MIP signal of the cosmic muons should improve with the LED corrections. The improvement gained with this procedure was not tested till now.

It is concluded from these studies that temperature correlated fluctuations can be corrected by means of a parameterised temperature dependence. The studies with the LED system show that remaining effects are below 0.5%. To study possible corrections with the second method, long term cosmics data or beam data runs has to be correlated with the LED shifts. These stability studies for longer time periods (order of months) are presently done with the MiniCal prototype.

Chapter 6

APD Studies

In this section the analysis of APD measurements are described. For APD readout tests, the MiniCal has been equipped with 33 APDs from Hamamatsu. These APDs have the same design as the APDs used in the CMS [25] electromagnetic calorimeter but the active area is reduced to 3×3 mm^2 (CMS uses 5×5 mm^2). A characterisation measurement of the used APDs has been performed to extract the APD gain dependency on voltage, temperature dependence and the capacitance. The measurement and results are described in section 6.1.1 and 6.1.2.
In section 6.2 MiniCal measurements in the testbeam are discussed.

6.1 APD Characterisation

6.1.1 APD Gain and Capacity

APDs are used as photodetectors with constant amplification as a precision light detector. The knowledge of gain with respect to the bias voltage is mandatory to set the best working region. The bias voltage should be set to high gain to reduce electronic noise and to improve the gain to dark current ratio. Above a certain bias voltage which is APD dependent, the dark current is growing faster than the gain. The APDs should be operated below this critical voltage.
The APDs have been tested at CERN with the setup used for quality measurements of CMS APDs [27]. The dark current $I_{dark}(U)$ and the current $I_{total}(U)$ with illumination have been measured versus the bias voltage. The capacity versus bias voltage has been measured also. The gain is defined as:

$$M(U) = \frac{I_{\text{total}}(U) - I_{\text{dark}}(U)}{< I_{\text{total}} >} \tag{6.1}$$

$<I_{\text{total}}>$ is the mean value at low voltages, for which the gain should be consistent with M=1. The gain dependence curves for the APDs used in these studies shows the

expected strong increase at high voltages above 400V (figure 6.1). Figure 6.1 shows two groups of APDs with different voltage dependences. The numbering scheme from Hamamatsu point to two different production cycles with different wafers. This could affect the depth of the doped layers of the active area leading to different gain curves. For readout purposes the gain for all APDs should be the same. Therefore the APDs

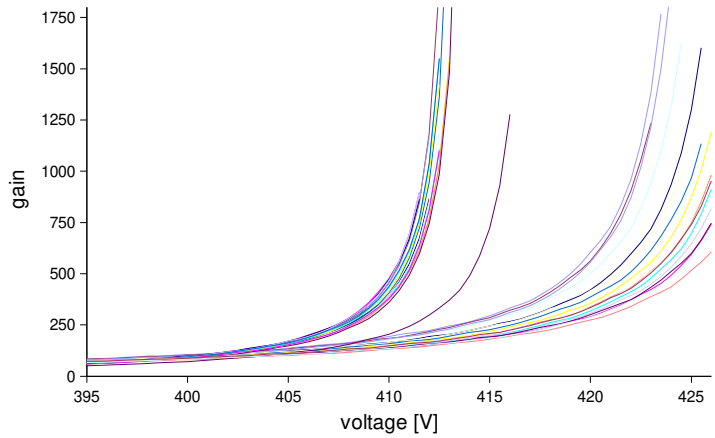

Figure 6.1: The gain versus bias voltage for the 33 used Hamamatsu 3×3 mm^2 APDs.

are divided in two groups set to different bias voltages on the preamplifier to reach equal gain.

The applied bias voltage on the APDs leads to a depleted area at the different doped

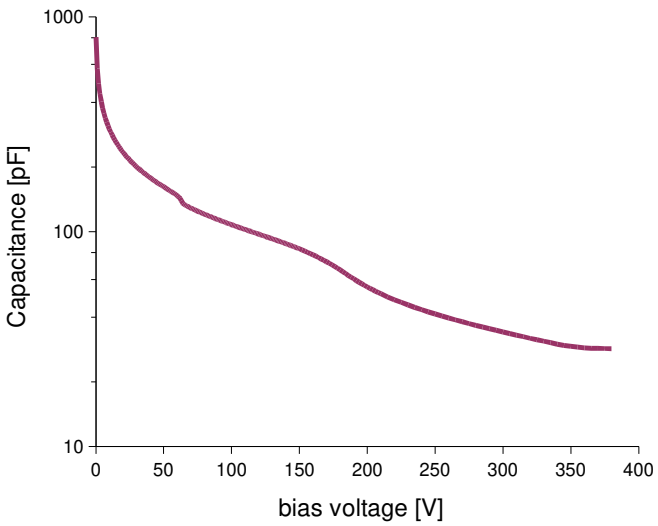

Figure 6.2: The capacitance for one Hamamatsu 3×3 mm^2 APD.

layers in the APD. In this region the amount of free electrons for conduction is reduced.

The depletion region acts as a capacitor. As the depleted region depends on the voltage, the capacitance of the APD also depends on the applied voltage. If the doped layer is fully depleted the capacitance should get almost independent of the applied bias voltage. This is the bias voltage setting needed to get the best quantum efficiency. As shown in figure 6.2 the bias voltage should be higher than $\approx 350\,\mathrm{V}$ to reach full depletion.
The capacitance of our APDs are below C=1 nF for a low bias voltage and are at C=20 pF for a bias voltage of V_{bias}=400 V which is our working point.

6.1.2 APD Homogeneity

If the APDs have an inhomogeneous gain depending on the position on the active area as considered in [26], the response to the scintillator light could be different for the three tiles connected to one APD. This would lead to a large systematic error in the energy measurement. A light mixer could be used to spread the scintillator light to the whole APD. The APD gain homogeneity is tested to study whether a light mixer is necessary.
The gain homogeneity is studied using a movable light source system which consists of a manually controlled x - y stage, a blue LED ($\lambda_{peak} = 450\,\mathrm{nm}$) and a clear fibre to guide the light to the APD. This produces a light spot of 0.5 mm in diameter. The APD gain has been measured for 12 illuminated points following the measuring scheme shown in figure 6.3(a).

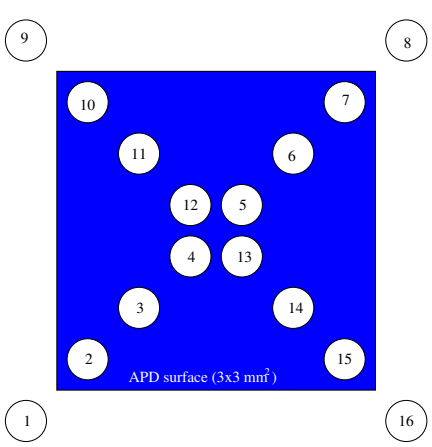

(a)

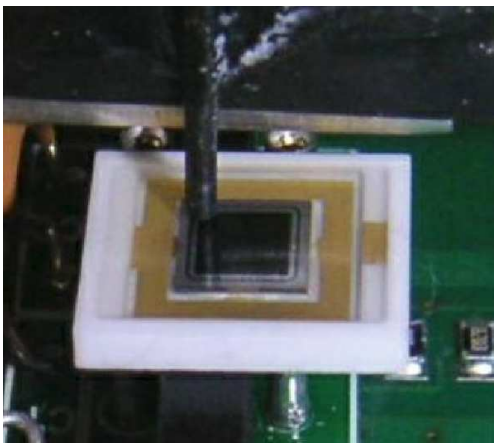

(b)

Figure 6.3: (a) Sketch of the homogeneity measurement procedure. The positions of the measurement points are shown. (b) Picture of the homogeneity measurement setup with APD and clear fibre.

The APD is readout with the Minsk preamplifier described in section 4.4 and the signals are digitised in a CAMAC ADC. About $10{\cdot}10^3$ events per point have been

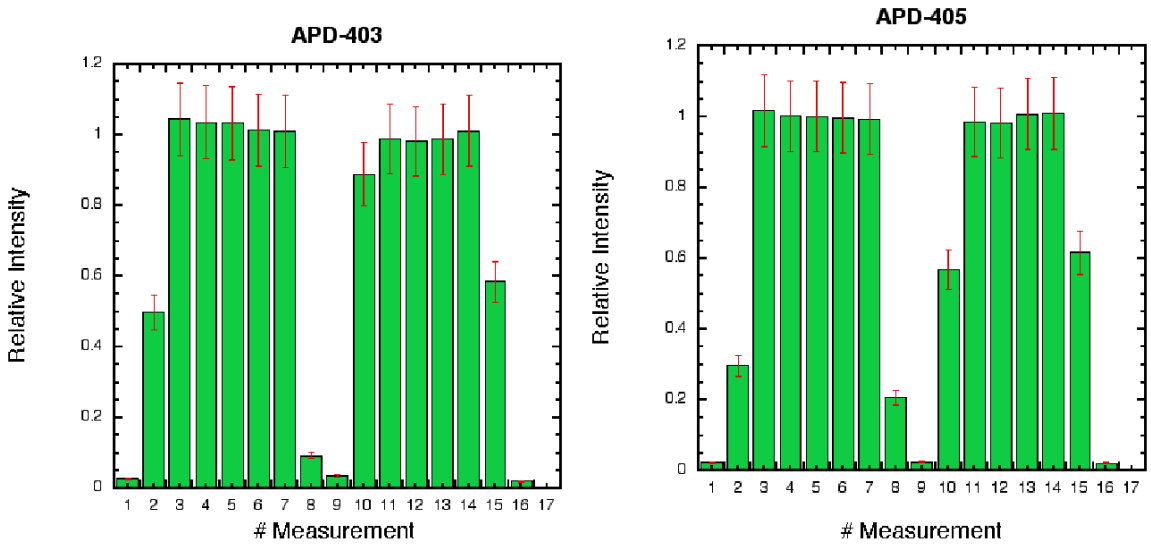

(a) (b)

Figure 6.4: Measured gain variation for 2 APDs at different positions. The gain is normalised.

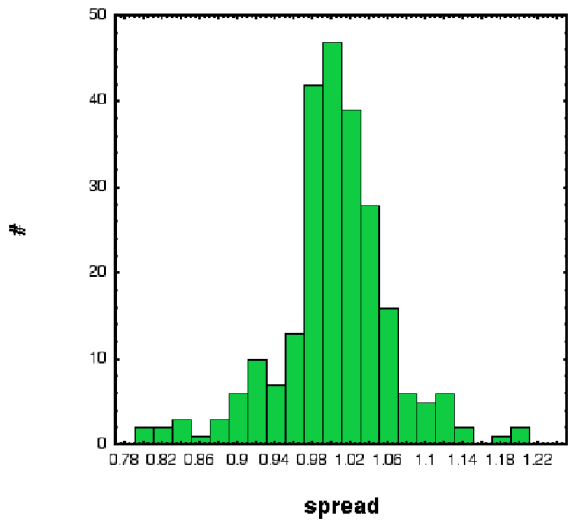

Figure 6.5: Distribution of all measured points. The mean value is at 1 the width is σ=0.03.

collected at a voltage of 400 V which gives a gain of $\approx$ 110.
Each APD has been tested separately. The data for each APD are normalised by averaging over all points above 75% with respect to the maximum for each APD. Sometimes parts of the illuminated spot exit the active area and thus, the signal is

decreased. In this case, the number of points showing the maximum light output is reduced as shown for point 2 and 15 for APD #403 in figure 6.1.2.
All tested APDs have a homogeneous gain distribution as shown in fig. 6.1.2 for 2 samples. The relative gain distribution for all measured points (fig. 6.5) shows a small variation of 3%, the APD active area is almost uniform. A readout with three fibres connected to one APD without light mixer is possible.

6.2 APD MiniCal Data

In this section the data analysis for APD measurements are described. The calibration procedure is explained, the shower shape compared to simulation and the linearity and energy resolution are determined.
Data has been taken with the APDs as photodetectors, as described in chapter 4. The MiniCal has been equipped with 12 cassettes of scintillating tiles and the APDs are connected via wave length shifting fibre. A positron beam of DESY II (see section 4.5) has been shot into the central stack of the MiniCal with a energy range from 1 GeV to 6 GeV.

6.2.1 MIP Calibration

For the APD measurements of linearity and energy resolution a calibration in terms of Minimum Ionising Particles (MIPs) has been performed. The calibration accounts for different light yields of individual scintillator tiles and the spread of the gain of the photodetectors. The calibration can be transformed into an absolute energy calibration using the simulation information of MIP energy deposited in a scintillator tile and the fraction of energy visible in the active layers.
The calibration has been performed with cosmic muons and with e^+ beam for photomultiplier tubes. The two methods give compatible results within the calibration accuracy [32]. The beam calibration is much faster than the calibration with cosmic muons. For APDs a calibration with the electron beam has been performed.
The calibration has been performed by moving the cassettes out of the absorber plates but still within the light tight MiniCal box. A Beam of 3 GeV positrons has been shot in the centre of each one of the 9 tile stacks. The data consists of 25k events for each calibration run.
The 12 cassettes have a total radiation length of 0.4 X_0. Thus most of the positrons move through the cassettes producing a MIP like signal in the stacked tiles and only some start to shower. To ensure the MIP traverses all 12 layers, a cut on the data is imposed to requires a MIP like signal in the last layer.
To validate the calibration procedure of all cassettes at the same time the last layer has been calibrated independently 6.6(b). The two calibration factors extracted with and without the 11 other layers in front are compared and found to agree within 4%.

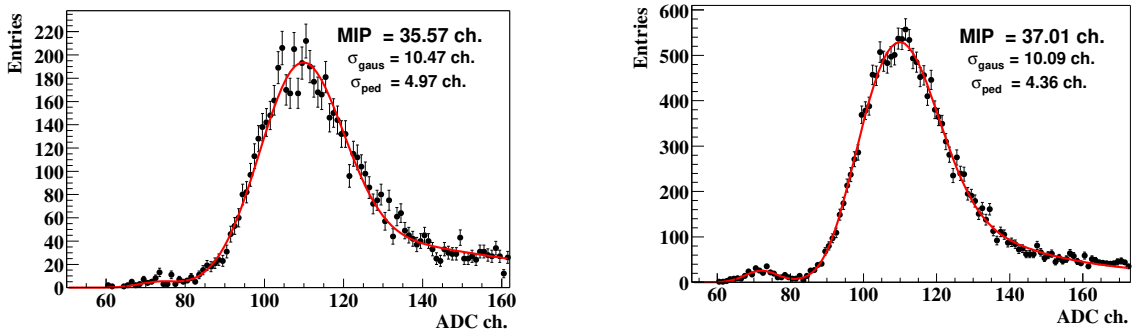

(a) (b)

Figure 6.6: MIP signal for the 12^{th} tile in the central stack as an example of MIP calibration at 3 GeV. (a) MIP peak with 11 cassettes in front. (b) MIP peak without 11 cassettes in front.

The MIP signal is fit with a linear combination of a Gaussian and a Landau function (fig. 6.6). The MIP amplitude for each tile is defined to be the difference between the the most probable value of the signal and the mean value of the noise peak.
The noise of the APD readout using the Minsk preamplifier is compared with the APD readout using the Prague preamplifier as well as with the photomultiplier readout by using the ratio of the MIP amplitude to the Gaussian width of the pedestal.

$$\frac{S}{N} \propto \frac{\text{MIP}}{\sigma_{\text{noise}}} \tag{6.2}$$

The average S/N ratio for APDs read out with the Minsk preamplifier is ≈ 9.5, for the Prague preamplifier the S/N is ≈ 6.6. The Prague preamplifier has about 1/3 more noise pickup. For the photomultiplier run a S/N of ≈ 17 and the SiPM have an even better ratio of ≈ 30. Due to the low gain of the APDs the signal is more distorted by electronics noise (from preamplifier and DAQ) and noise pick up in the cables than the photomultiplier.
The ratio S/σ_{MIP} expresses the separability between signal and noise peak, which is a useful quantity for setting a limit for a possible threshold cut. The $S/\sigma_{\text{MIP}} \approx 5$ for the Minsk preamplifier, 3.7 for the Prague preamplifier, 3.7 for SiPMs and ≈ 3.3 for the photomultipliers. This can be explained with the higher noise of the Prague preamplifier with respect to the Minsk preamplifier and the fact, that the quantum efficiency of the APD is much higher than the photomultiplier or SiPM, which give a higher intrinsic noise and a relatively larger photoelectron fluctuation.
All systems satisfy to separate the MIP position from pedestal.
The MIP calibration stability is evaluated by comparing two MIP calibrations performed at a week distance. The ratio of the calibration factors for the central 12 tiles is shown in figure 6.7. Within 1% the two calibrations agree.

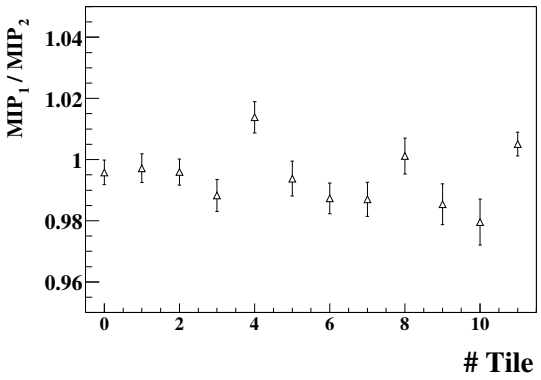

Figure 6.7: Ratio of two sets of calibration factors for the core tiles.

6.2.2 Detector Simulation

The electron shower evolution has been simulated by implementing the MiniCal geometry into the GEANT4 [31] framework. The stainless steel has been implemented with a density of $8\,\mathrm{g/cm^3}$ as measured in the laboratory. The cassettes are implemented as 2.5 mm aluminium and 5 mm scintillating plastics. The WLS-fibre loops are included to test possible inhomogeneities. A total of 12 layers of steel and absorber are simulated.
For an ideal detector response an energy resolution of $18\%/\sqrt{E}\oplus\ 2\%$ is obtained. The constant term of 2% is due to shower leakage from the last layer of the calorimeter [32]. For a more realistic simulation, detector physics is implemented according to the scheme presented in figure 6.8. The deposited energy per tile is expressed in MIPs and a conversion into photoelectrons is applied using the photodetector efficiency. The number of photoelectrons per MIP are extracted from APD signal width. Poissonian fluctuations of the photoelectrons is added. The photoelectrons are converted to an ADC output. The ADC channels per photoelectron are extracted from the position of the MIP peak position. The beam energy spread described in section 4.5 has been included in the simulation.

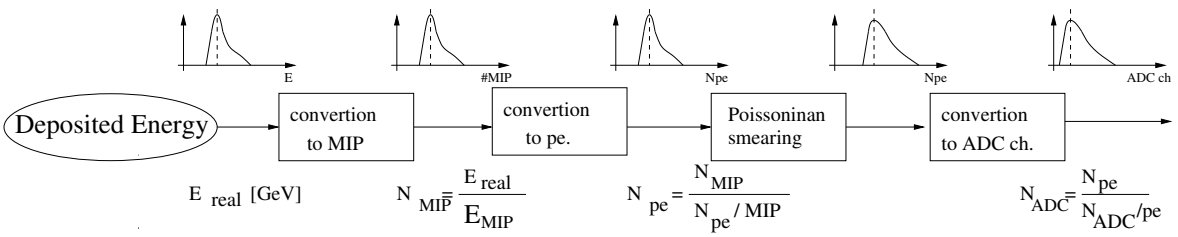

Figure 6.8: Flow chart of simulation implementation of photodetector physics.

6.2.3 Shower Shape Comparison

The main task of the final detector will be shower reconstruction. For this, the shower shape must be determined as precisely as possible. As the electromagnetic shower simulation prediction is almost perfect, this showers are used to verify the modelling of detector effects and the correct treatment of calibration.

A tile by tile comparison between 1 to 6 GeV e^+ shower data and simulation pre-

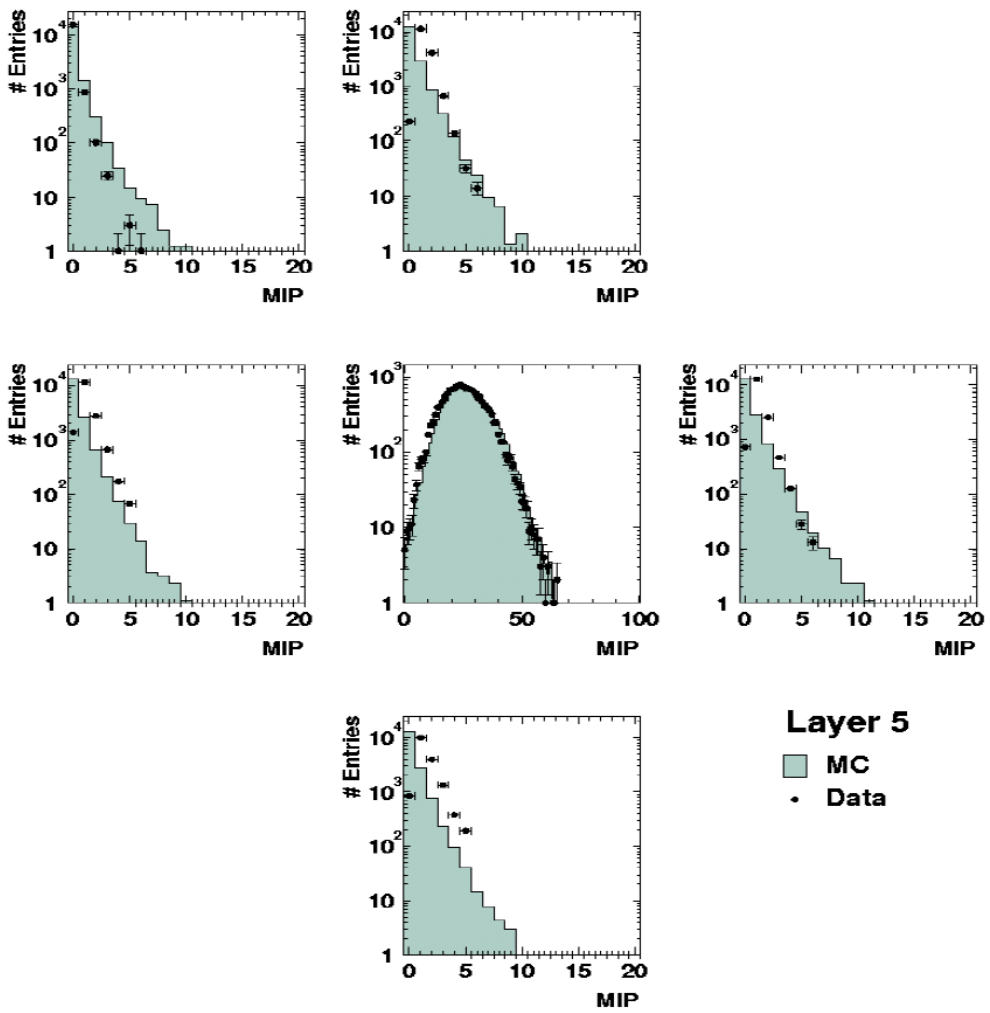

Figure 6.9: Transversal shower shape for 5 GeV positrons in the 5^{th} layer read out by APDs. Three corners are not equipped with APDs. The filled region corresponds to simulation while data is shown as black points.

dictions has been performed. Almost all energy is deposited in the centre tiles while the surrounding tiles contain little energy. This is shown in figure 6.9 for 5 GeV. The energy deposited is expressed in numbers of MIPs. About 90% of energy is deposited

in the centre tiles, almost independent of the used beam energy. This is predicted by simulation.

Three corners are not equipped with photodetectors. The figure 6.9 shows, that the

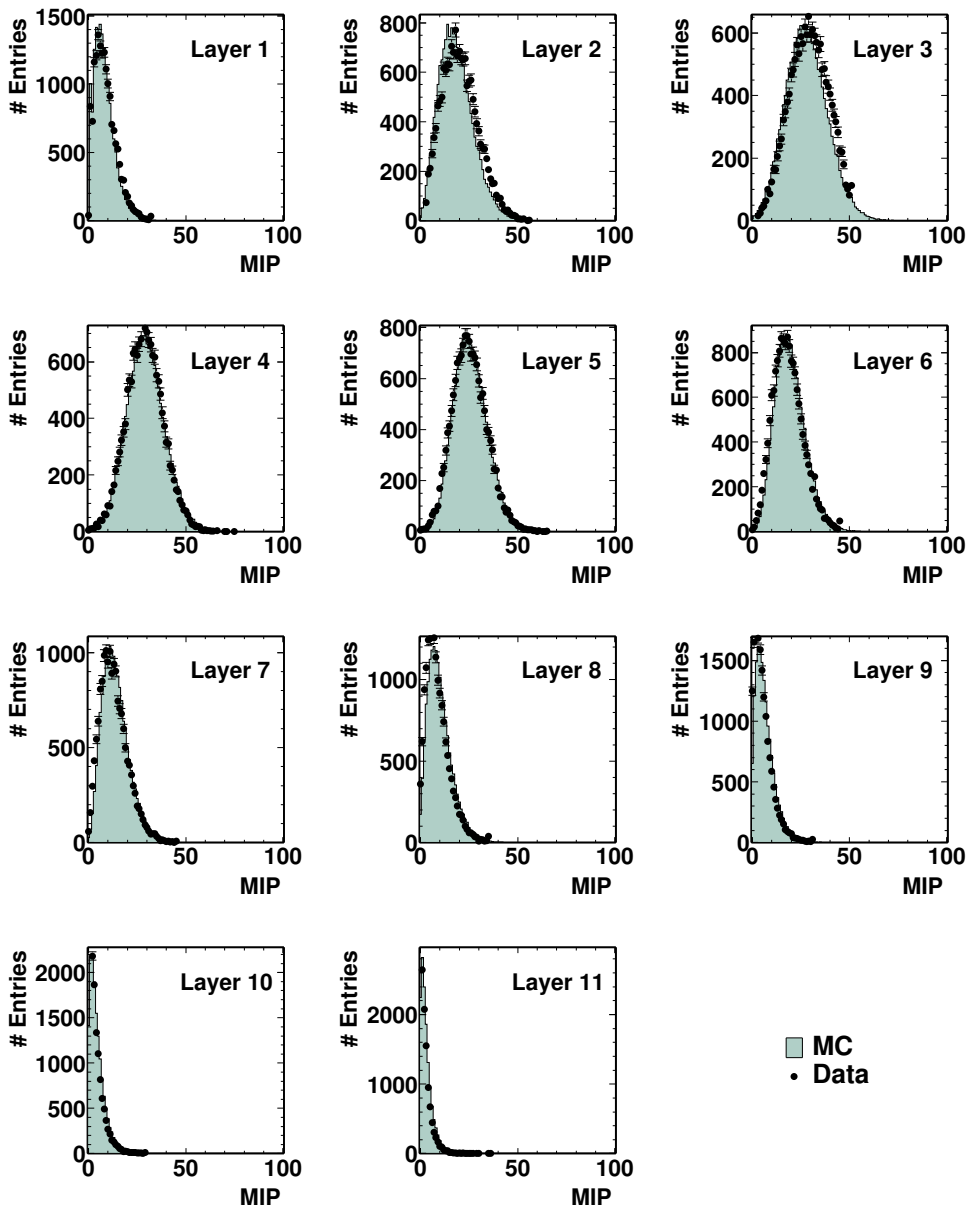

Figure 6.10: Longitudinal shower shape for 5 GeV positron shower developing in the central stack read out by APDs. The filled histogram corresponds to simulation while data is shown as black line.

energy deposition not covered in this case is minor.

Shower comparison in the central stack should fit best to simulation because statistical effects play a minor role. The longitudinal development of the electromagnetic shower in the central stack of the MiniCal is shown in figure 6.10. The simulation gives a good description of the shower development. In the first 3 layers, the deposited energy is underestimated. This could be caused by a slightly different number of photoelectrons per MIP in the simulation than in the data. The shower shape is independent of the used preamplifier. SiPM and Photomultipliers give comparable results as shown in [32].

6.2.4 Systematic Errors

The systematic error is estimated in this section. There are several contributions to the systematic uncertainties. In the calibration there is an uncertainty of 4% due to the calibration procedure of shooting a positron beam into 12 cassettes, as explained in section 6.2.1. The fitting uncertainties are expected to be less than 1% as two independent analyses of the data with two different fitting procedures, one fitting a Gauss and a Landau distribution and the second only fitting a Gaussian function give the same results. The APD temperature dependence affects mostly the long term stability as mentioned in chapter 5. The short term runs for calibration and energy scans have an uncertainty due to temperature shifts of $\approx 0.5\%$. The calibration reproducibility show an uncertainty of less than 1%.
The uncertainty due to tile non-uniformity has been measured in [32] to be of the order of 2%. The photodetector-preamplifier system non-linearity is 1% for both preamplifiers, as shown in figure 6.12(b).
All this errors, summed in quadrature, lead to an overall systematic error in the order of 5%.

6.2.5 Linearity and Energy Resolution

The energy deposited on each tile, calibrated in MIPs, is summed event by event. The energy distribution for particle energies of 1 to 6 GeV is shown in figure 6.11. The energy deposited in the single readout corner is multiplied by four to account for the missing energy information in the three corners not read out. The deposited energy should increase proportional to the energy of the incident e^+. The Gaussian mean value of the deposited energy in MIPs is plotted versus the expected energy in figure 6.12(a) and a linear curve is fit. The slope could be affected by saturation effects or leakage effects. As leakage is small and saturation is not expected for APDs, the slope for all detectors should be the same.
For the Minsk preamplifier the slope is 36.1 ± 0.3 MIPs/GeV. This is comparable to the results extracted using the Prague preamplifier which measured an energy deposition of 36.7 ± 0.3 MIPs/GeV. The simulation, where the detector response and beam energy spread is implemented as mentioned in section 6.2.2, predicts 36.0 ± 0.3 MIPs/GeV.

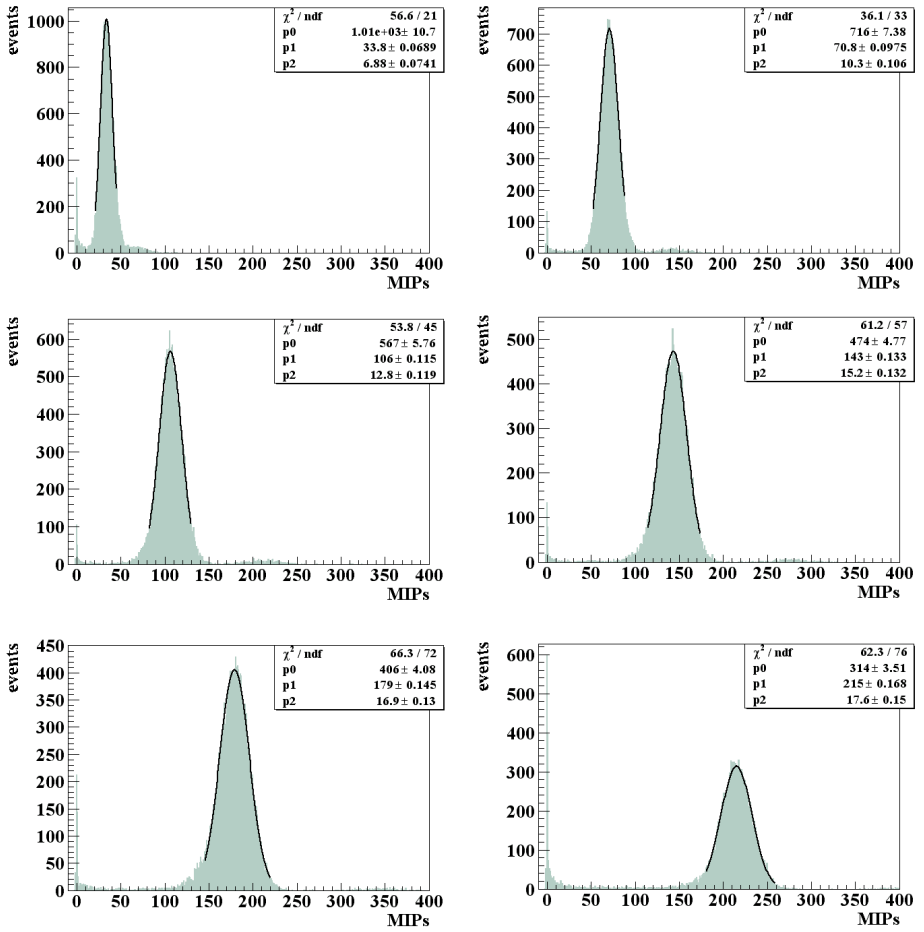

Figure 6.11: Energy sum for energies from 1 GeV to 6 GeV.

As expected different S/N of the preamplifiers has no influence on the linearity, as both preamplifiers are able to separate the MIP peak from the noise peak resulting in a good calibration.

The energy resolution is determined as the spread of energy relative to the most probable deposited energy. The energy resolution is shown in figure 6.13 for both preamplifiers and the simulation. A word of caution is needed to remind that the MiniCal structure is a prototype for a hadronic calorimeter tested here with electromagnetic showers.

An energy resolution of $\approx 20.5\%$ is obtained with both preamplifiers. There is only small sensitivity to the constant term, the constant term is within the errors comparable with zero. Table 6.1 gives an overview of the results for the different measurements. There is excellent agreement between the different readout technics and with the simulation.

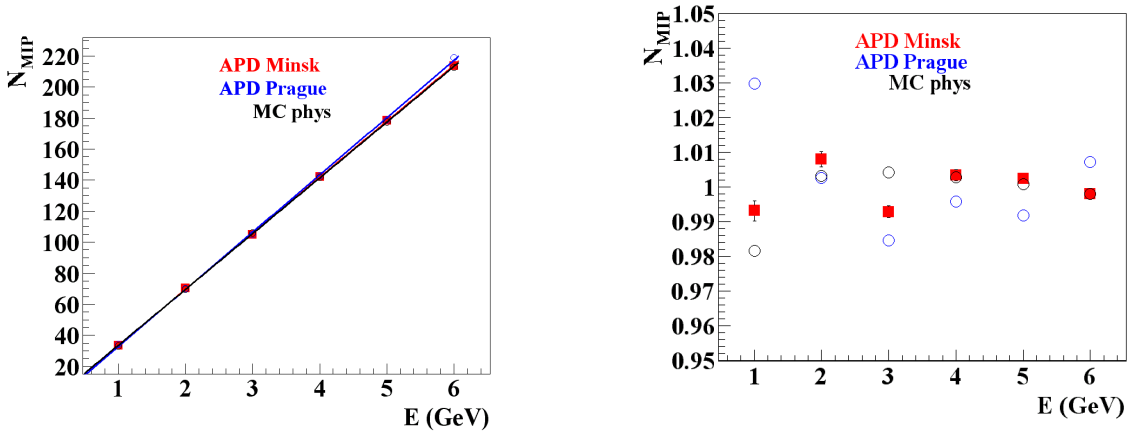

(a) (b)

Figure 6.12: (a) Linearity for two runs with different preamplifiers. They both show the same linear behaviour. (b) Deviation from the linear curve for both preamplifiers and simulation.

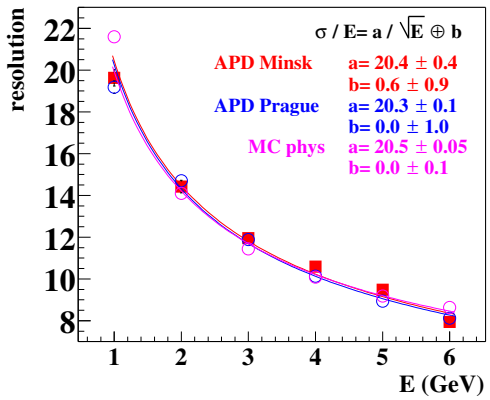

Figure 6.13: Energy resolution.

detector	stochastic term	constant term
APD with Minsk preamp.	20.4 ± 0.4	0.6 ± 0.9
APD with Prague preamp.	20.3 ± 0.1	0.0 ± 1.0
Simulation for APDs	20.5 ± 0.05	0.0 ± 0.1
Photomultiplier [32]	21.1 ± 1.0	1.3 ± 4.1
SiPM [32]	20.7 ± 0.7	2.6 ± 1.3

Table 6.1: Comparison of the energy resolution measurements for different photodetectors in the MiniCal and the APD simulation.

Chapter 7

Summary and Outlook

Measurements with APDs as readout devices have been performed with the MiniCal, a scintillator steel sandwich calorimeter for testbeam measurements.
Due to the low gain at which APDs are operated, the noise introduced by the preamplifier has been expected to worsen the response compared to other photodetectors. Two preamplifiers have been tested with different characteristics and intrinsic noise. The results in terms of linearity and energy resolution are found to be insensitive to the type of preamplifier used. Furthermore, the APD data are in reasonable agreement with previous measurements taken with photomultipliers and SiPM [32].
The energy deposited in each tile of the MiniCal has been calibrated in numbers of MIPs. The calibration procedure has a reproducibility of 4%. Temperature and gain changes in the setup in between calibrations can be monitored by an LED system with a precision better than 1%.
Corrections of long term temperature induced changes of the APD gains are possible, using a parameterisation of the temperature dependence of the gain.
The MiniCal operation has provided valuable experience for the design, construction and operation of a physics prototype to test different hadronic shower models at low energies and optimise the particle flow algorithms. The prototype is foreseen to be completed early next year and will be tested with an electromagnetic calorimeter prototype in an hadron beam for further studies on hadronic showers reconstruction.
The LED monitoring system will be integrated into the physics prototype and will be extended to monitor also the optical readout chain. This is done by injecting UV light into the scintillator cells with an optimised LED light distribution system. In this way the response of the full system of scintillator tiles, wavelength shifting fibres and photodetectors is monitored.
The physics prototype will test the hardware on the grand scale to be qualified for the linear collider detector, but delivers also data for the optimisation of the particle flow concept. There is also the unique opportunity to get improved knowledge on the hadronic shower development in the low energy range.

Bibliography

[1] Memorandum to PRC, from the proposal 01/02, DESY Hamburg, Memo-01, CALICE collaboration, October 2001.

[2] R. Wigmans: Calorimetry - Energy Measurement in Particle Physics, Oxford University Press (2000)

[3] TESLA - The Superconducting Electron-Positron Linear Collider with an Integrated X-Ray Laser Laboratory, Technical Design Report, DESY 2001-011 (2001).

[4] N. Toge, ed. [JLC Design Study Group], JLC design study, KEK-REPORT-97-1 (1997).

[5] T.O. Raubenheimer, ed. [NLC ZDR Design Group], Zeroth order design report for the Next Linear Collider, SLAC-R-0474 (1996).

[6] DESY PRC-R&D 02/02, Linear Collider Detector R&D, Aug. 2002.

[7] The CALICE collaboration: CAlorimeter for the LInear Collider with Electrons, http://polywww/in2p3.fr/tesla/calice.html

[8] K.Ishii et al.: Performance studies of a lead-scintillation fiber calorimeter prototype for the linear collider detector,NIM A385(1997)215.

[9] C. Issever, Development of an alternative weighting method for the H1 calorimeter, DESY-FH1-96-06

[10] V. L. Morgunov, Energy-flow method for multi-jet effective mass reconstruction in the highly granulated TESLA calorimeter, *Proc. of the APS/DPF/DPB Summer Study on the Future of Particle Physics (Snowmass 2001)* ed. N. Graf, eConf **C010630** (2001) E3041.

[11] V. L. Morgunov, Two particle separation with Tile HCAL, Talk given at International Conference on Linear Colliders, Paris, 19-23 April, 2004

[12] C.W. Fabjan, Calorimetry in High-energy Physics, in: Experimental Techniques in Nuclear and Particle Physics, T. Ferbel ed., World Scientific, 1991.

[13] The CALICE collaboration homepage: http://polywww.in2p3.fr/flc/calice.html

[14] DESY PRC-R&D 00/02, Construction and test of an Electromagnetic Calorimeter prototype, 2000.

[15] Characteristics and use of Si APD (Photo diode),Technical information SD-28, Hamamatsu

[16] Hamamatsu Multi Anode Assembly H8711 and h8711-10, Hamamatsu

[17] F. Sauli, Development and applications of gas electron multiplier detectors, Nucl. Instrum. Meth. A **505** (2003) 195.

[18] B. Voigt: A Test Setup for the Investigation of Charge Transfer Processes of a GEM Based TPC, University of Hamburg (Apr. 2004)

[19] Sören Reiche: Studies for the Optical Read-Out of a Hadronic Tile-Fiber-Calorimeter for TESLA, University of Hamburg (Nov. 2001)

[20] Albert Einstein: Über einen die Erzeugung und Verwandlung des Lichtes betreffenden heuristischen Gesichtspunkt, Annalen der Physik 17,132-148 (1905)

[21] Roman Pöschel: private communications.

[22] Jaroslav Cvach: private communications.

[23] S. Eidelman et al.: Phys. Lett. B592, 1 (2004)

[24] Urs M. Heller et al.: Numerical analysis of the Higgs mass triviality bound, Nucl. Phys., B405:555-573 (1993)

[25] K. Deiters *et al.*,CMS ECAL APD quality assurance facility,11-15 Sep 2000 *Prepared for 6th Workshop on Electronic for LHC Experiments, Cracow, Poland*

[26] R. S. Gilmore et al., Avalanche photo diodes (APD) as proportional devices, BR-HEP-94-3 *Presented at International Conference on Applications of Photonic Technology (ICAPT 94), Toronto, Canada, 21-23 Jun 1994*

[27] A. Karar, J. C. Vanel and Y. Musienko, Characterisation of avalanche photodiodes for calorimetry applications, Nucl. Instrum. Meth. A **428** (1999) 413.

[28] J. Janoth, Das Calibrationssystem CAM für das neue Kalorimeter SpaCal das Detektors H1 bei HERA und Analyse erster Daten, HD-IHEP-96-17

[29] ROOT, An object oriented data analysis framework, http://root.cern.ch/

[30] CAEN Power Supply manual.

[31] S. Agostelli *et al.*, Nucl. Instr. Meth. A **506**(2003) 250.

[32] V. Andreev *et al.*, Scintillator tile hadronic calorimeter with SiPM readout for a linear collider detector, to be published in Nucl. Instr. Meth.

Danksagung

An dieser Stelle möchte ich mich bei allen Menschen bedanken, die mich bei dieser Arbeit direkt und indirekt unterstützt haben.
Mein Dank gilt Prof. Rolf-Dieter Heuer für die Möglichkeit in seiner Forschungsgruppe arbeiten zu dürfen. Die Arbeit in der Gruppe hat mir sehr viel Spaß gemacht und ich habe viel gelernt. Außerdem möchte ich Prof. Götz Heinzelmann für die Zweitkorrektur danken.
In der CALICE Kollaboration habe ich eine gute internationale Zusammenarbeit erfahren, die ich als sehr aufbauend empfand.
In der Arbeitsgruppe möchte ich besonders Erika Garutti danken, die sich auch mit meinen Versuchen einer englischen Fassung der Diplomarbeit auseinandergesetzt hat. Die gute Atmosphäre an meinem Arbeitsplatz verdanke ich Markus Ball, Thorsten Kuhl und Peter Wienemann. Bedanken möchte ich mich auch bei Felix Sefkow und Marius Groll, die mir mit Rat und Tat zur Seite standen.
Meiner Familie danke ich besonders. Auch in Zeiten, in denen der Kontakt eher sporadisch war, haben sie mich immer unterstützt. Reges Interesse an meiner Arbeit haben auch meine Großeltern. Dieses hat mir sehr viel Freude bereitet.
Zum Schluß möchte ich mich noch meinen Freunden bedanken, insbesondere bei Annette, Daniel, Sandra, Michael, Stefan und Bastian, die die Zeit so erlebnisreich gestaltet und mir Rückhalt gegeben haben.

Erklärung

Hiermit versichere ich, die Arbeit selbständig und nur unter Verwendung der angegebenen Quellen und Hilfmittel verfasst zu haben. Ich gestatte die Veröffentlichung dieser Arbeit.